Chapter 3

DFT virtual screening identifies rhodium-amidinate complexes as active homogeneous catalysts for methane to methanol oxidation

Reproduced in part with permission from Fu, R.; Nielsen, R. J.; Goddard, W. A. III; Fortman, G. C.; Gunnoe, T. B. *ACS Catalysis*, submitted for publication. Unpublished work © 2014 American Chemical Society. Also includes original work.

3.1 Abstract

In the search for new organometallic catalysts for the low temperature selective conversion of CH_4 to CH_3OH, we apply quantum mechanical virtual screening to select the optimum combination of ligand and solvent on rhodium to achieve low barriers for CH_4 activation and functionalization to recommend for experimental validation. We report quantum mechanical predictions (including implicit and explicit solvation) of the mechanisms for various bidentate and tridentate $\mathrm{Rh}^{\mathrm{III}}$ complexes to catalytically activate and functionalize methane, using trifluoroacetic acid (TFAH) or water as a solvent. Our most notable results include the design of a $\mathrm{Rh}^{\mathrm{III}}(\mathrm{NN}^{\mathrm{F}})$ ((NN^{F} = bis(*N*-pentafluorophenyl) pentafluorobenzylamidinate) complex, with a methane activation transition state barrier of $\Delta G^{\ddagger} = 27.6$ kcal/mol in TFAH, and a $\mathrm{Rh}^{\mathrm{III}}$(bisq) ((bisq) = bis(quinolinyl)benzene) complex, with a methane activation transition state barrier of $\Delta G^{\ddagger} = 33.4$ kcal/mol in TFAH. To close the catalytic cycle, the functionalization of methylrhodium intermediates was also investigated, involving carbon-oxygen bond formation *via* $\mathrm{S_N2}$ attack by solvent, or $\mathrm{S_R2}$ attack by a vanadium oxo. In addition, we have found a correlation between CH_4 activation barriers and rhodium-methyl bond energies that allow us to predict the activation transition state energies for future ligands as well.

3.2 Introduction

The facile, selective, and direct conversion of methane into methanol has long been a goal of industrial chemists [1]. Molecular compounds in solution have long been investigated as potential catalysts for this transformation, as they are typically well-defined, easy to characterize and model, and operate under relatively mild conditions. Whereas much previous work has been done on Pt and Pd catalysts [2, 3], in this chapter we focus on rhodium due to its well-documented nature as an effective C−H activating metal [4] and whose lower electronegativity may allow it to avoid poisoning by coordinating media.

Our initial calculations found that using neutral tridentate pincer ligands (L_3) resulted in neutral $L_3Rh(TFA)_3$ resting states. In order for such complexes to activate methane, a TFA ligand must be both protonated and removed to create an open coordination site. The frequent result was that the overall methane activation energy (i.e. energy of the transition state minus energy of the resting state) was too high to be feasible. Thus, to provide the best candidates for experiments, we shifted our attention to bidentate and monoanionic ligands, which are expected to favor Rh^{III} states that would incorporate a labile, protonated TFAH solvent molecule, thus removing the extra energy penalty for protonation. Bidentate and tridentate ligands were chosen to facilitate redox processes which interconvert square-planar and octahedral coordination environments. Thus we initially examined four classes of ligands that we thought might be prove effective while likely not too hard to synthesize:

- bis(*N*-phenyl)benzylamidinate (NN);
- (*N*-phenyl)acetaldiminyl quinolate (ONN);
- bis(pyridyl)(m)ethanesulfonate (DP$\frac{\text{M}}{\text{E}}$S);
- bis(pyrrolyl)quinolinyl phosphine (PN);

and two solvents: water and trifluoroacetic acid, due to their pH range and oxidative stability. We then embarked on quantum mechanical (QM) virtual screening to select the optimum combinations of ligand and solvent to recommend for experimental validation. Here we used density functional theory (DFT) at the B3LYP and M06 levels, including both implicit and explicit solvation, for systematic searches over possible reactions mechanisms for CH_4 activation and for functionalization.

We found that rhodium complexed with the bidentate bis(*N*-phenyl) benzylamidinate (NN) ligand was the most promising in our initial screen. We then designed a new ligand, bis(*N*-pentafluorophenyl) pentafluorobenzylamidinate (NN^F), essentially an electron-poor version of (NN), that we found to be even more promising, with lower transition state barriers for both methane activation and Rh−Me functionalization. In addition, we also designed more and less electron-donating variations of the (ONN) ligand; and broadened our investigation to a fifth ligand class, bis(quinolinyl)benzene (bisq), that was expected to have further reduced functionalization barriers.

Our efforts culminated in two complexes,

- $\mathrm{Rh^{III}}$(bis(*N*-pentafluorophenyl) pentafluorobenzylamidinate), denoted as $\mathrm{Rh^{III}(NN^F)}$; and
- $\mathrm{Rh^{III}}$(bis(quinolinyl) benzene), denoted as $\mathrm{Rh^{III}}$(bisq);

that can catalytically activate and functionalize methane, using TFAH or water as a solvent. The first case, $\mathrm{Rh^{III}(NN^F)}$, leads to a transition state barrier of $\Delta G^{\ddagger} = 27.6$ kcal/mol at 298 K for methane activation in TFAH (35.0 kcal/mol in water), the lowest we have found using $\mathrm{Rh^{III}}$. The barrier for functionalization is $\Delta G^{\ddagger} = 36.8$ kcal/mol at 298 K for TFAH (29.7 kcal/mol in water). The second case, $\mathrm{Rh^{III}}$(bisq), leads to a transition state barrier of $\Delta G^{\ddagger} = 33.4$ kcal/mol at 298 K for methane activation in TFAH, and $\Delta G^{\ddagger} = 32.0$ kcal/mol at 298 K for Rh−Me functionalization in TFAH, also among the lowest we have found using $\mathrm{Rh^{III}}$. For $\mathrm{Rh^{III}}$ complexes with neutral transition states, we find that increasing the electron-withdrawing nature of the ligands decreases barriers for both activation and functionalization. Thus, the only condition opposing even less donating ligands (i.e. lower barriers) is catalyst stability.

This chapter should be of great interest to experimentalists who can now focus on these two ligands in TFAH and water to validate and further optimize these systems.

3.3 Materials and Methods

All quantum mechanical calculations were carried out using the Jaguar software version 7.6 developed by Schrödinger Inc. [5]. Geometry optimizations were carried out on initial guess structures, and vibrational frequencies were calculated to confirm the optimized geometries as intermediates or transition states and to construct a free energy profile. Solvation energies were calculated using the PBF Poisson-Boltzmann implicit continuum solvation model [6] in Jaguar, with a dielectric constant of 8.55 and a probe radius of 2.451 Å for TFAH and 80.37 and 1.40 Å for water. Explicit waters were added into the calculations of aqueous $\mathrm{Rh(NN^F)}$ (two explicit waters per aqua ligand) for more accurate solvation modeling.

Geometry optimization and vibrational data were calculated using the B3LYP density functional [7] with a smaller basis set, whereas single point gas-phase and solvated energies were calculated using the M06 functional [8] and a larger basis set. Here the "smaller basis set" consists of a modified double-ζ Los Alamos basis set and pseudopotential [9] that includes f functions for rhodium [10], and the 6-31G** basis set [11] for the other atoms; whereas the "larger basis set" consists of the triple-ζ Los Alamos basis set and pseudopotential (LACV3P**++) modified to include f functions and diffuse functions for rhodium, and the 6-311G**++ basis set [12] for the other atoms. For orbital analysis, the Pipek-Mezey localization procedure was used [13].

Rather than specify a particular chemical oxidant, we adopted a consistent electrostatic potential for electrons to determine the free energy changes of redox reactions. A value of 1.23 V *vs.* SHE, the standard potential for the reduction of oxygen at pH = 0 and 25°C ($O_2(g) + 4\,H^+(aq) + 4\,e^-(aq) \longrightarrow 2\,H_2O(\ell)$), was adopted for models in trifluoroacetic acid. For water, the pH was taken as 7 and the potential thus reduced to 0.817 V; this was calculated using the equation $E = E^\circ - \Delta G/n\mathcal{F}$ where $\mathcal{F}$ is Faraday's constant and $\Delta G = kT \ln Q = kT \cdot \mathrm{pH} \cdot \ln 10$. The free energy of the electron was then calculated using the equation $G = -\mathcal{F}(E + 4.28\text{ V})$ where 4.28 V represents the absolute potential of the SHE reference, yielding electron free energies of -127.1 and -117.5 kcal/mol, respectively [14]. The free energy of the proton was taken as -260 kcal/mol in TFAH and -279.80 kcal/mol in pH = 7 water [15]. The free energy for each molecular species in solution was calculated using the formula

$$G = E_{\text{gas}} + \Delta G_{\text{solv}} + \text{ZPE} + H_{\text{vib}} + 6kT - T[S_{\text{vib}} + 0.54(S_{\text{trans}} + S_{\text{rot}} - 14.3\text{ e.u.}) + 7.98\text{ e.u.}]$$

where the last term is an empirical approximation for the change in the translational and rotational entropy of the molecule between the gas phase and the solution phase (due to the finite librational frequencies) derived from Wertz [16]. For gas phase molecules (methane, methanol at 498.15 K, and for the purposes of this study methyl trifluoroacetate), we assumed that equilibration between the dissolved gas and the headspace occurred at a much faster timescale than the reactions in question; leading to $\Delta G_{\text{gas}\rightarrow\text{solv}} = 0$. Thus, the free energy of such gas molecules can be simply calculated using the formula

$$G = G_{\text{gas}} = E_{\text{gas}} + \text{ZPE} + H_{\text{tot}} - TS_{\text{tot}}.$$

We simulated methanol in the gas phase at 498.15 K and the solution phase at room temperature by adding the empirical hydration free energy of -3.2 kcal/mol [17] to the gas phase free energy.

For pure liquids (e.g., trifluoroacetic acid and water), the Gibbs free energy was calculated using the formula

$$G_{\text{liquid}} = E_{\text{gas}} + \text{ZPE} + H_{\text{tot}} - TS_{\text{tot}} + \Delta G_{\text{gas}\rightarrow\text{liquid}}$$

where $\Delta G_{\text{gas}\rightarrow\text{liquid}} = G_{\text{liquid}} - G_{\text{gas}}$ (1 atm) is the free energy of condensation to liquid from 1 atm gas. We can solve for this by noting that

$$\Delta G_{\text{gas}\rightarrow\text{liquid}} = \Delta G_{\text{exp}} + \Delta G_{\text{gas}\rightarrow\text{solv}}$$

where $\Delta G_{\text{exp}} = G_{\text{gas}}(P) - G_{\text{gas}}(1\text{ atm})$ is the expansion of the gas from 1 atm to the vapor pressure P, and $\Delta G_{\text{gas}\rightarrow\text{solv}}$ is the condensation of gas to liquid. Since a liquid is by definition at equilibrium

Temperature	Trifluoroacetic acid			Water		
	A	B	C	A	B	C
298.15 K	3.33963	1267.252	-52.958	5.40221	1838.675	-31.737
323.15 K	3.33963	1267.252	-52.958	5.20389	1733.926	-39.485
348.15 K	3.33963	1267.252	-52.958	5.07680	1659.793	-45.854
373.15 K	3.33963	1267.252	-52.958	5.08354	1663.125	-45.622
398.15 K	3.33963	1267.252	-52.958	3.55959	643.748	-198.043
423.15 K	3.33963	1267.252	-52.958	3.55959	643.748	-198.043
448.15 K	3.33963	1267.252	-52.958	3.55959	643.748	-198.043
473.15 K	3.33963	1267.252	-52.958	3.55959	643.748	-198.043
498.15 K	3.33963	1267.252	-52.958	3.55959	643.748	-198.043

Table 3.1. Antoine equation parameters used for trifluoroacetic acid and water at each temperature point investigated. Numbers taken from [18] and are set such that P will be measured in bar.

with its vapor pressure, $\Delta G_{\text{gas}\to\text{solv}} = 0$, and we thus have

$$\Delta G_{\text{gas}\to\text{liquid}} = G_{\text{gas}}(P) - G_{\text{gas}}(1\text{ atm}) = RT \ln\left(\frac{P}{1\text{ atm}}\right).$$

We can find the vapor pressure P at a given temperature using the Antoine Equation:

$$\log_{10} P = A - \frac{B}{C+T},$$

where the empirical parameters A, B, and C vary with the solvent and temperature range and were taken from table 3.1. Calculations were performed at nine temperature levels spaced by 25 K from 298.15 K to 498.15 K.

The $\text{S}_\text{R}2$ attack involving $\text{OV}^{\text{V}}\text{Cl}_3$ converts two singlets to two doublets, and hence the transition states feature spin contamination ($S^2 > 0$) while representing an overall singlet. Structures that did not feature such spin contamination were considered to be transition states for an alternative $\text{S}_\text{N}2$ attack that forms $\text{MeOV}^{\text{III}}\text{Cl}_3^-$ and a Rh^{I} species, all of which were higher in energy.

3.4 Results

The most common oxidation state of rhodium is +III, but oxidation states from 0 to +VI have been observed [19]. While previous work has focused on the C−H activation ability of Rh^{I} [3]b, our current results center on a Rh^{III} resting state. This is due to the requirement that the desired process operate above the $\text{CH}_4/\text{CH}_3\text{OH}$ redox couple (0.59 V *vs.* SHE at pH = 0) and below the reduction potential of O_2 in the reaction conditions, which favor higher oxidation states.

Scheme 3.1 shows hypothetical catalytic cycles for the activation and functionalization of methane. Starting from an inorganic Rh^{III} resting state (**1**), we investigated the C−H activation of methane following the displacement of a TFAH solvent molecule (**$2^\ddagger$**) to form a Rh$^{\text{III}}$-methyl organometallic species (**3**). Starting with (**3**), there are several pathways to functionalization:

1. **III-I**: $\text{S}_\text{N}2$ attack (**$4^\ddagger$**) by the conjugate base of the solvent to form methyl trifluoroacetate and a Rh$^{\text{I}}$ species (**5**), which is reoxidized to the inorganic Rh$^{\text{III}}$ resting state (**1**). In all cases investigated we found that this $\text{S}_\text{N}2$ attack occurs on a five-coordinate Rh complex, with the neutral solvent *trans* to the methyl group dissociated in the transition state. This is consistent with previous work by Goldberg et al. implicating five-coordinate platinum intermediates [20];
2. **III-II**: $\text{S}_\text{R}2$ attack (**$6^\ddagger$**) by a metal-oxo species to form a metal-methoxy species and a Rh$^{\text{II}}$ species (**7**) *via* methyl radical transfer. Both of these are then reoxidized by one electron, to the metal-oxo species and methanol and to the inorganic Rh$^{\text{III}}$ resting state (**1**), respectively. Here, OVCl_3 was used as a model metal-oxo capable of one-electron reduction, even though it would likely hydrolyze in these solvents. We are developing stable metal oxo reagents optimized for this reaction mechanism [21] and use OVCl_3 here as a computationally simple model. The $\text{S}_\text{R}2$ transition state for Rh(NN) involves a five-coordinate Rh complex as well. For the Rh(NN$^{\text{F}}$) case, the transition states retain weak interactions with the neutral *trans* ligand, with an elongated Rh$-$O bond distance of 2.472 Å for TFAH and 2.228 Å for water. This is presumably due to the increased electrophilicity of the metal center in the Rh(NN$^{\text{F}}$) complexes;
3. **III-IV-II**: Oxidation to a Rh$^{\text{IV}}$ species (**8**) followed by $\text{S}_\text{N}2$ attack (**$9^\ddagger$**) generating a Rh$^{\text{II}}$ species (**7**), which is then further oxidized back to the Rh$^{\text{III}}$ resting state (**1**). This route was only investigated for the Rh(NN^{x}) and Rh(DP$\frac{\text{M}}{\text{E}}$S) complexes, which had both kinetically accessible activation transition states and thermodynamically accessible Rh$^{\text{IV}}$ intermediates. In all cases investigated we found that this $\text{S}_\text{N}2$ attack occurs on a six-coordinate Rh complex, presumably due to the increased electrophilicity of the Rh$^{\text{IV}}$ center. The six-coordinate Rh complexes have elongated Rh$-$O bond distances to the neutral *trans* ligand (e.g., 2.377 Å for Rh(NN), 2.379 Å for Rh(NN$^{\text{F}}$), and 2.255 Å for Rh(NN$^{\text{F}}$) in water).

In all cases, the energy of reoxidation was calculated assuming a potential of 1.23 V *vs.* SHE, i.e. with O_2 as the terminal oxidant. However, in practice it may be necessary to use intermediate oxidants as well, although that is beyond the scope of this study.

A system which can proceed around any of these cycles with a global activation barrier below approximately 36 kcal/mol at 200°C is of academic interest, as transition state theory gives a turnover frequency (TOF) of roughly 1 hr^{-1} at 1 atm CH_4 for such a process. Achieving an industrially relevant TOF on the order of 1 s^{-1} requires a global barrier of 29 kcal/mol, although greater pressures of CH_4 would increase this limit [22].

We screened complexes of rhodium with the following ligands, as depicted in Figure 3.1:

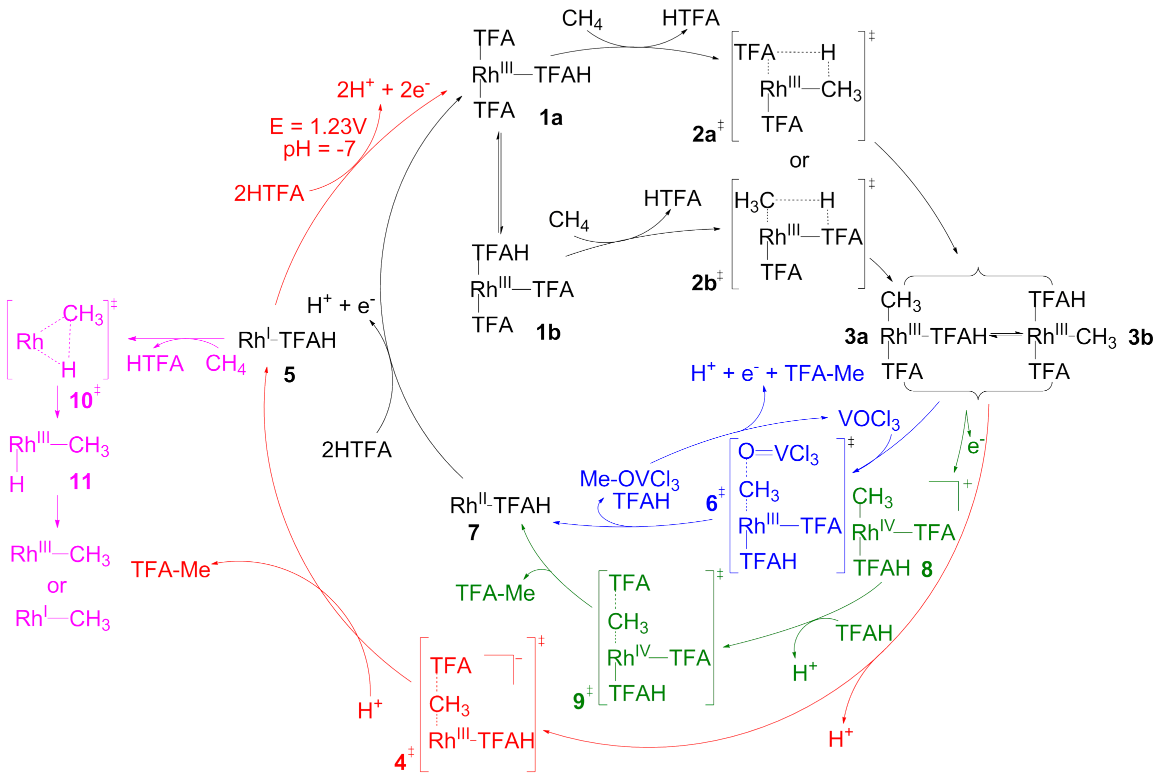

Scheme 3.1. Hypothetical catalytic cycle for the activation and functionalization of methane. This shows several potential routes, including III-I (red), III-II (blue), and III-IV-II (green), which are further described in the text. In addition, a fourth possibility, I-III (purple), involves the direct C−H activation (**10**‡) by a $\mathrm{Rh^{I}}$ species (**5**) to a $\mathrm{Rh^{III}}$ hydride methyl (**11**). However, given the oxidizing nature of the reaction conditions, we do not anticipate this to be a fruitful pathway, as any catalytic cycle involving a $\mathrm{Rh^{I}}$-(III) cycle would likely suffer from the fact that oxidation of **5** to **1** would act as a thermodynamic sink. Hence, this last option was not pursued to the same extent in this investigation.

- the bis(*N*-phenyl)benzylamidinate (NN) ligand and its fluorinated analogue (NN^F);
- the (*N*-phenyl)acetaldiminyl quinolate (ONN) ligand and its related (ONN^F) and (ONN^{NMe_2}) ligands;
- the bis(pyridyl)methanesulfonate (DPMS) and bis(pyridyl)ethanesulfonate (DPES) ligands;
- the bis(pyrrolyl)quinolinyl phosphine (PN) ligand; and
- the bis(quinolinyl)benzene (bisq) ligand, its di- and tetrafluorinated analogues ($bisq^{F_2}$) and ($bisq^{F_4}$), and its di- and tetramethylated analogues ($bisq^{Me_2}$) and ($bisq^{Me_4}$).

Figure 3.1. The rhodium-ligand complexes screened. For each complex, the Rh^I form in TFAH is shown here, but full catalytic cycles were computed. The best kinetics were predicted for the $Rh(NN^F)$ and Rh(bisq) complexes.

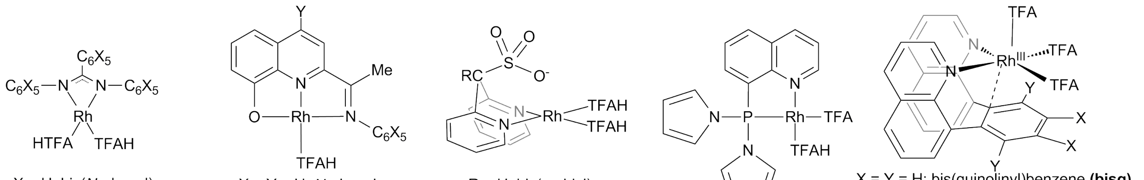

X = H: bis(*N*-phenyl) benzylamidinate **(NN)**
X = F: bis(*N*-perfluorophenyl) perfluorobenzylamidinate **(NN^F)**

X = Y = H: *N*-phenyl acetaldiminyl quinolate **(ONN)**
X = F, Y = H: *N*-perfluorophenyl acetaldiminyl quinolate **(ONN^F)**
X = H, Y = NMe_2: *N*-phenyl acetaldiminyl dimethylaminoquinolate **(ONN^{NMe2})**

R = H: bis(pyridyl) methanesulfonate **(DPMS)**
R = Me: bis(pyridyl) ethanesulfonate **(DPES)**

bis(pyrrolyl) quinolinyl phosphine **(PN)**

X = Y = H: bis(quinolinyl)benzene **(bisq)**
X = F, Y = H: bis(quinolinyl) difluorobenzene **($bisq^{F2}$)**
X = Y = F: bis(quinolinyl) tetrafluorobenzene **($bisq^{F4}$)**
X = Me, Y = H: bis(quinolinyl) dimethylbenzene **(bis^{Me2})**
X = Y = Me: bis(quinolinyl) tetramethylbenzene **($bisq^{Me4}$)**

For each of these ligands complexed with rhodium, we generated catalytic cycles in the template of Scheme 3.1. For the (DPMS), (PN), and (ONN^x) family of ligands, we found that either the methane activation energy or the methyl functionalization energy (or both) were too high for effective catalysis (Table 3.2). However, we found lower numbers for the (NN^x) family of ligands, on which we have decided to focus our discussion.

3.4.1 The Rh(NN) complexes in TFAH

Scheme 3.2 shows the calculated free energies of Rh(NN) complexes in trifluoroacetic acid solvent. Note that all free energies are referenced to the resting state, $[(NN)Rh^{III}(TFA)_4]^{2-}(H^+_{ax})_2$, which is highlighted by a purple box. Hence, although the resting complex is regenerated at the end of the catalytic cycle, the new free energy is −13.7 kcal/mol at 298 K, because this is the energy change of the overall equation $CH_4 + TFAH \longrightarrow TFA{-}Me + 2\,H^+ + 2\,e^-$; and thus all energies at the second cycle would be −13.7 kcal/mol lower.

Oxidation of the inorganic Rh^I species to inorganic Rh^{III} species is highly favorable, from 40 to 50 kcal/mol downhill, depending on the temperature and the charge of the species. We conclude that

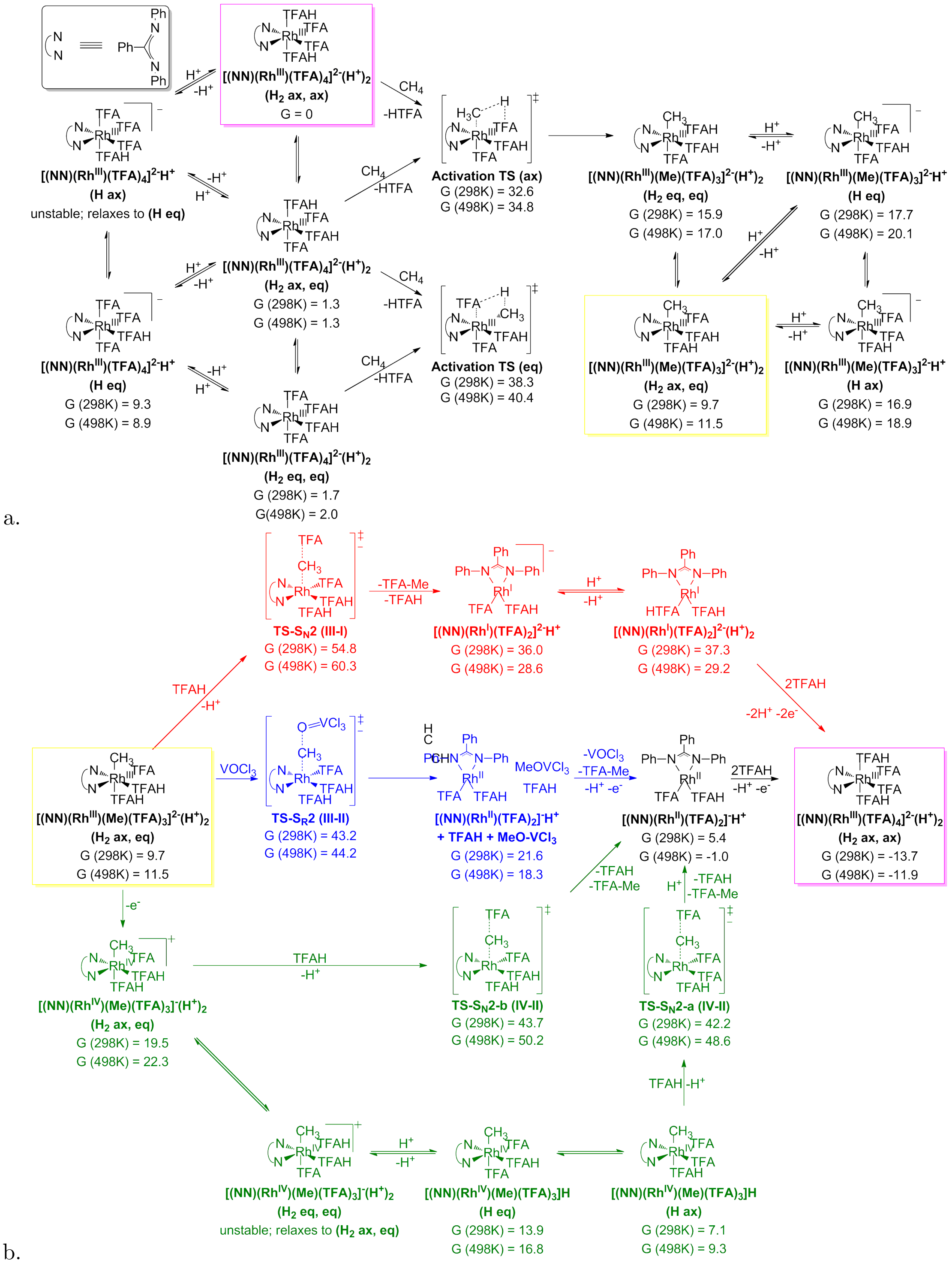

Scheme 3.2. (a) Activation of methane using Rh(NN) complexes in TFAH; and (b) the subsequent functionalization. Red denotes the III-I functionalization pathway; blue the III-II pathway, and green the III-IV-II pathway. Free energies (kcal/mol) are referenced to the resting state, $[(\mathrm{NN})\mathrm{Rh}^{\mathrm{III}}(\mathrm{TFA})_4]^{2-}(\mathrm{H}^+_{\mathrm{ax}})_2$. The resting state is highlighted by a purple box, and the key methyl intermediate, $[(\mathrm{NN})\mathrm{Rh}^{\mathrm{III}}(\mathrm{Me}_{\mathrm{ax}})(\mathrm{TFA})_3]^{2-}(\mathrm{H}^+_{\mathrm{ax}})(\mathrm{H}^+_{\mathrm{eq}})$, is highlighted by a yellow box.

TS type	TS	Rh(NN)	Rh(NN^F)	Rh(ONN)	Rh(ONN^F)	Rh(ONN^{NMe_2})	Rh(DPMS)	Rh(DPES)
Activation	Me_{ax}	32.6/34.8	27.6/29.6	37.2/39.8	35.8/37.8	38.7/41.2	38.0/40.2	41.0/44.0
	Me_{eq}	38.3/40.4	33.7/36.3	37.9/40.7	38.1/40.1	40.0/42.9	33.9/36.2	35.6/38.4
Functionalization	(III-I)	54.8/60.3	42.7/48.2	44.2/49.3	41.7/45.8	46.7/52.6	46.6/51.3	53.8/59.3
	(III-II)	43.2/44.2	38.1/40.0	40.4/42.5	39.1/40.8	41.4/43.4	41.0/41.6	45.5/47.4
	(III-IV-II)	42.2/48.6	36.8/43.6	N/A	N/A	N/A	49.3/56.3	49.9/57.1

TS type	TS	Rh(PN)	Rh(bisq)	Rh($bisq^{F_2}$)	Rh($bisq^{F_4}$)	Rh($bisq^{Me_2}$)	Rh($bisq^{Me_4}$)
Activation	Me_{ax}	40.1/43.0	38.3/40.7	39.3/42.4	40.4/43.0	38.8/41.9	40.7/44.4
	Me_{eq}	35.0/37.7	33.4/35.8	36.4/39.4	38.2/40.9	32.8/35.9	34.3/37.5
Functionalization	(III-I)	38.3/43.8	31.8/37.8	32.3/38.4	30.2/35.0	35.0/41.9	38.0/45.5
	(III-II)	47.7/56.9	32.0/33.7	31.8/33.6	33.7/35.3	35.7/38.3	38.9/42.0

Table 3.2. Lowest activation and functionalization energies for each series of Rh-ligand complexes in TFAH. Detailed cycles for the (NN^x) family of ligands are found in Schemes 3.2 and 3.3. Detailed cycles for the (ONN^x) family of ligands are found in Schemes 3.9 through 3.11. Detailed cycles for the ($DP\frac{M}{E}S$) family of ligands are found in Schemes 3.12 through 3.14. Detailed cycles for the (PN) ligand are found in Schemes 3.15 and 3.16. Detailed cycles for the ($bisq^x$) family of ligands are found in Schemes 3.17 through 3.20. For each entry, the first number is at 298 K and the second at 498 K. Not all III-IV-II transition states were calculated. All free energies in kcal/mol.

the III-I S_N2 attack pathway is not likely. Indeed, the activation barrier for this is a prohibitively high 54.8 kcal/mol at room temperature (Figure 3.2b). In addition, we also conclude that a I-III pathway involving methane activation by Rh^I is not likely due to the oxidation potential of the Rh^I species.

The remaining viable pathways all involve methane activation by the inorganic Rh^{III}(NN) complex to form a Rh^{III}(NN)$-$Me species. We were initially gratified to see that thermodynamically the methyl species is not very endergonic. We were even more intrigued to find that the methane activation transition state barrier is only 32.6 kcal/mol at 298 K (Figure 3.2a), making it the most accessible barrier that we had found for Rh^{III} complexes in TFAH (Table 3.2).

In contrast, neither the III-II (Figure 3.2c) nor the III-IV-II (Figure 3.2d) functionalization pathways seemed as promising. Although further oxidation to a Rh^{IV}(NN)$-$Me species was roughly thermoneutral, the barrier to reductive functionalization was 42.2 kcal/mol. The oxidation from Rh^{III} to Rh^{IV} was effective in lowering the global S_N2 barrier from 54.8 to 42.2 kcal/mol. To explain the high functionalization barrier for S_N2 attack, we note that this may be due to the high energy or low chemical activity of trifluoroacetate ion in solution. Since TFA^- is necessary as the attacking nucleophile, a higher pH may be employed to lower this barrier before a deprotonated intermediate becomes the new resting state.

Due to the unusually low barrier for methane activation, we did not want to dismiss this ligand framework. Rather, our efforts focused on how potential modifications on the (NN) ligand might lower the functionalization barrier. Reasoning that a more electronegative ligand may inductively increase the electrophilicity of the rhodium-methyl bond and make nucleophilic attack more likely, we decided to investigate Rh complexes with the fluorinated analogue bis(*N*-pentafluorophenyl) pentafluorobenzylamidinate (NN^F) ligand.

Figure 3.2. Rh(NN) transition state structures. (a) methane activation: Rh1-C36 2.273 Å, C36-H19 1.365 Å, H19-O10 1.321 Å, Rh1-C36-H19 64.624°, C36-H19-O10 155.492°. (b) Rh(III-I) S_N2 attack: Rh1-C60 2.431 Å, C60-O65 1.936 Å, Rh1-C60-O65 176.680°, Rh1-O53 3.473 Å. (c) Rh(III-II) S_R2 attack: Rh1-C60 2.368 ÅC60-O65 1.995 Å, Rh1-C60-O65 175.541°, Rh1-O53 3.171 Å. (d) Rh(III-IV-II) S_N2 attack: Rh1-C60 2.138 Å, C60-O64 2.263 Å, Rh1-O53 2.377 Å, Rh1-C60-O64 168.802°, C60-Rh1-O53 164.984°.

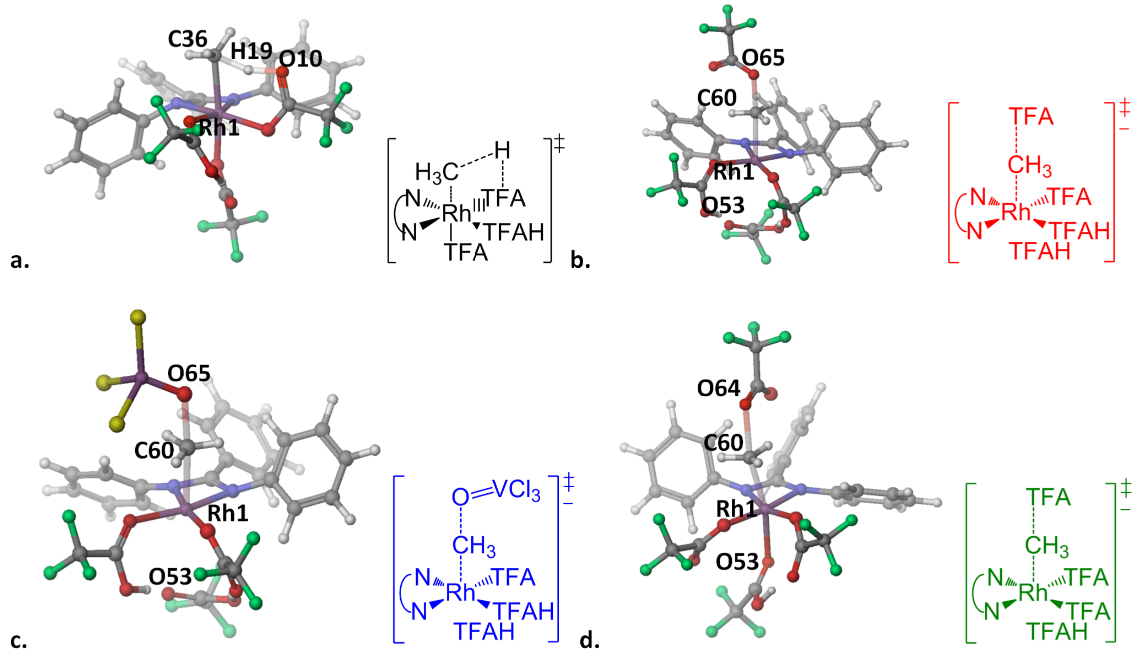

3.4.2 The Rh($\mathbf{NN^F}$) complexes in TFAH

Compared to the analogous Rh(NN) complexes, the fluorinated Rh(NN^F) complexes (Scheme 3.3) show some marked differences in free energies. Many of these differences can be attributed to the much higher electron-withdrawing character of the (NN^F) ligand. For instance, the Rh^I(NN^F) species is 13.3 kcal/mol more stable to oxidation than the corresponding Rh^I(NN) species. In the same way, the S_N2 functionalization barrier on the III-I path is 12.1 kcal/mol lower. This is due to the highly electron-withdrawing (NN^F) ligand, which stabilizes lower oxidation states. Unfortunately, this effect is not sufficiently large for us to consider the III-I or I-III pathways. Other thermodynamic effects of fluorine atom substitution include increased acidity of all the complexes (i.e. stabilization of the anionic species by 4-8 kcal/mol), an increased stabilization of the $Rh^{III}-Me$ species (by about 8 kcal/mol), and a decreased stabilization of the $Rh^{IV}-Me$ species (by about 20 kcal/mol relative to $Rh^{III}-Me$.)

The barrier for methane activation, already relatively low for the Rh(NN) case, was even lower for the Rh(NN^F) case, at only 28.7 kcal/mol at 298 K (Figure 3.3a). However, the real test of the utility of the (NN^F) ligand is its effectiveness in aiding the functionalization step. It lowers the global III-I S_N2 barrier from 54.8 to 42.7 kcal/mol and the isolated S_N2 barrier (from the $Rh^{III}-Me$ intermediate) to 40.8 from 45.1 kcal/mol (Figure 3.3b). It raises the neutral III-IV-II S_N2 barrier by raising the Rh^{IV} intermediate energy. Hence, we put our hopes into the (NN^F) ligand lowering the barrier for a net anionic III-IV-II S_N2 or a III-II S_R2 attack (Figure 3.3c,d). And indeed it does: the new global S_N2 and S_R2 barriers of 36.8 and 38.1 kcal/mol, respectively, approach the target values.

3.4.3 The Rh($\mathbf{NN^F}$) complexes in water

Another method that may lower transition state barriers is switching the solvent, and therefore the nucleophile, to water. This has the practical advantage that any commercialized process will have greater simplicity if carried out in water as opposed to a strong acid. Hence, we investigated the same Rh(NN^F) complexes in water.

The thermodynamic profile for Rh(NN^F) complexes in water (Scheme 3.4) is very promising: the Rh^{III}(NN^F)-methyl, Rh^{IV}(NN^F)-methyl, and Rh^{II}(NN^F) species are all stabilized relative to the inorganic Rh^{III}(NN^F) reference state. Hence, whereas for the TFAH solvent case a thermodynamic barrier must be climbed in each catalytic step, in water each step is either thermodynamically downhill or approximately neutral.

In Scheme 3.4, all energies are referenced to the lowest inorganic Rh^{III} state, $[(NN^F)Rh^{III}\text{-}(OH)_4]^{2-}(H^+_{ax})(H^+_{eq})$, which is highlighted by a purple box. This is to keep consistent with the practices in Schemes 3.2 and 3.3, where the lowest inorganic Rh^{III} state is also the resting state. However, in this case the organometallic Rh^{III}(NN^F)-methyl complexes are stabilized to such an

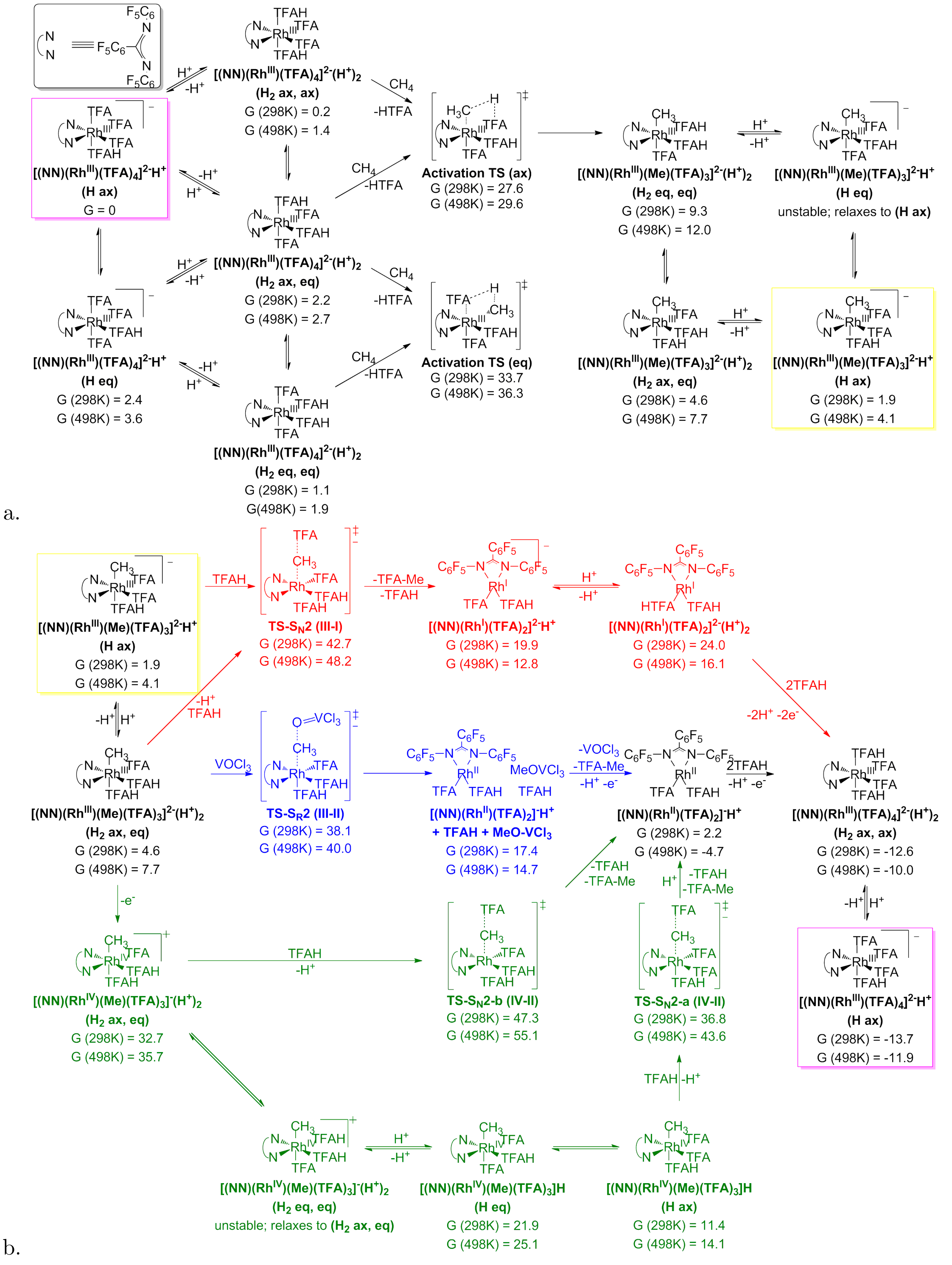

Scheme 3.3. (a) Activation of methane using Rh(NN^F) complexes in TFAH; and (b) the subsequent functionalization. Red denotes the III-I functionalization pathway; blue the III-II pathway, and green the III-IV-II pathway. Free energies (kcal/mol) are referenced to the resting state, $[(NN^F)Rh^{III}(TFA)_4]^{2-}(H^+_{ax})_2$. The resting state is highlighted by a purple box, and the key methyl intermediate, $[(NN^F)Rh^{III}(Me_{ax})(TFA)_3]^{2-}(H^+_{ax})$, is highlighted by a yellow box.

Figure 3.3. Rh(NN$^{\mathrm{F}}$) transition state structures. (a) methane activation: Rh1-C61 2.267 Å, C61-H19 1.365 Å, H19-O10 1.321 Å, Rh1-C61-H19 63.875°, C61-H19-O10 157.549°. (b) Rh(III-I) S$_{\mathrm{N}}$2 attack: Rh1-C60 2.368 Å, C60-O65 2.021 Å, Rh1-C60-O65 176.330°, Rh1-O53 3.265 Å. (c) Rh(III-II) S$_{\mathrm{R}}$2 attack: Rh1-C60 2.399 ÅC60-O65 1.935 Å, Rh1-O53 2.472 Å, Rh1-C60-O65 172.164°, C60-Rh1-O53 168.496°. (d) Rh(III-IV-II) S$_{\mathrm{N}}$2 attack: Rh1-C60 2.259 Å, C60-O64 2.156 Å, Rh1-O53 2.379 Å, Rh1-C60-O64 159.539°, C60-Rh1-O53 169.220°.

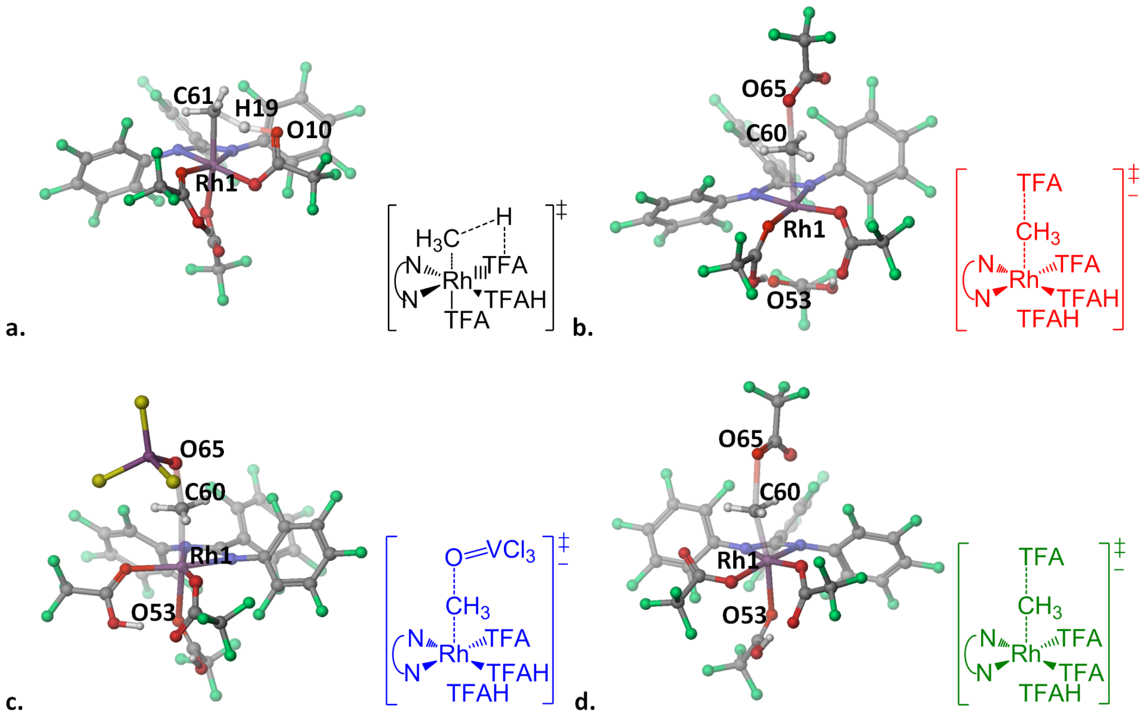

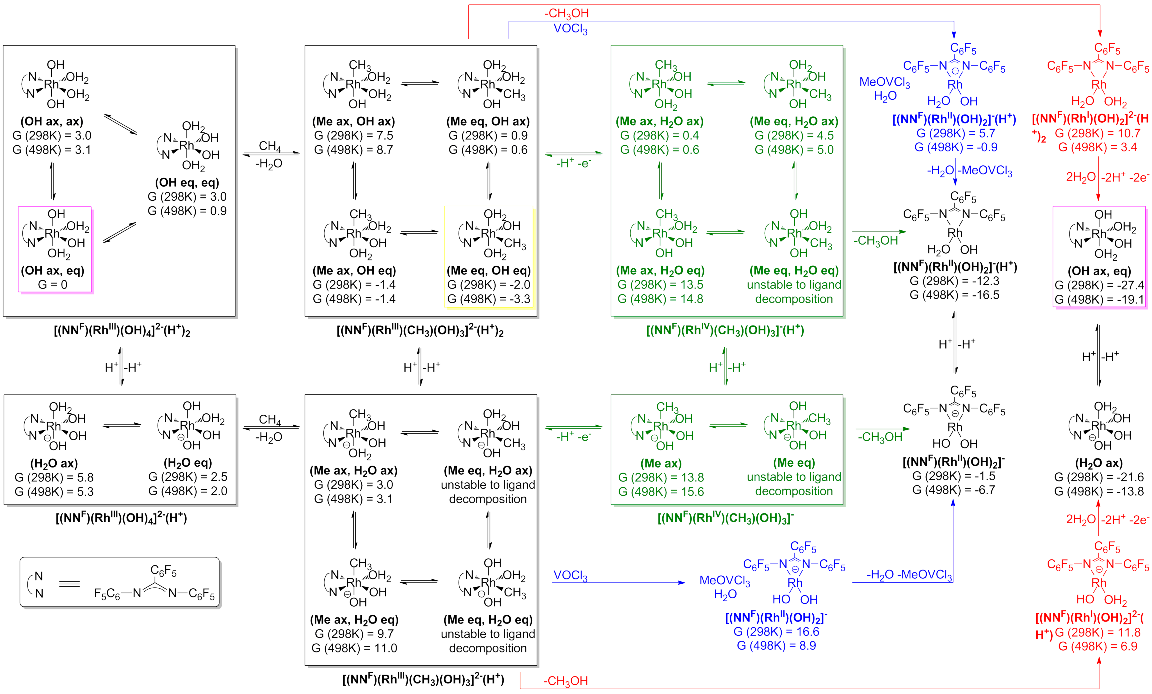

Scheme 3.4. Thermodynamic profile for the activation and functionalization of methane using Rh(NN^F) complexes in water. This chart is meant to be read from left to right; the first row contains the pathway through neutral species and the second row through anionic species. Red denotes the III-I functionalization pathway; blue the III-II, and green the III-IV-II pathway. All free energies (kcal/mol) are at pH = 7 and referenced to the lowest inorganic Rh^{III} state, $[(NN^F)Rh^{III}(OH)_4]^{2-}(H^+_{ax})(H^+_{eq})$, highlighted by a purple box; whereas the key methyl intermediate and true resting state, $[(NN^F)Rh^{III}(Me_{eq})(OH)_3]^{2-}(H^+_{ax})_2$, is highlighted by a yellow box.

extent that the true resting state is now $[(NN^F)Rh^{III}(Me_{eq})(OH)_3]^{2-}(H^+_{ax})_2$, which is highlighted by a yellow box and is analogous to the key methyl intermediate referenced in Schemes 3.2 and 3.3. The practical consequence is that the barrier to CH_4 activation is properly referenced to the lowest inorganic Rh^{III} state, whereas the barrier to methyl group functionalization ought to be referenced to the true resting state.

Having verified that the $Rh(NN^F)$ catalytic system in water was thermodynamically feasible, we sought accessible transition states for both the methane activation and functionalization steps. For methane activation, we began by assuming that the activation would take place *via* electrophilic substitution with a *cis* hydroxo ligand acting as a proton acceptor (Scheme 3.5). We then found transition states, starting from both neutral and anionic species, with the methane and the interacting hydroxo in every possible configuration with respect to the (NN^F) ligand. Our lowest transition state barrier of 35.0 kcal/mol at 298 K occurs with the methyl group forming in the axial position, donating its extra proton to an equatorial hydroxo ligand and *trans* to an axial hydroxo ligand (Figure 3.4a). This is significantly higher than in the TFAH solvent case, but still within the limits of feasibility. We examined the possible role of a concerted reaction with a bridging water molecule, but we did not see a decrease in the transition state energy.

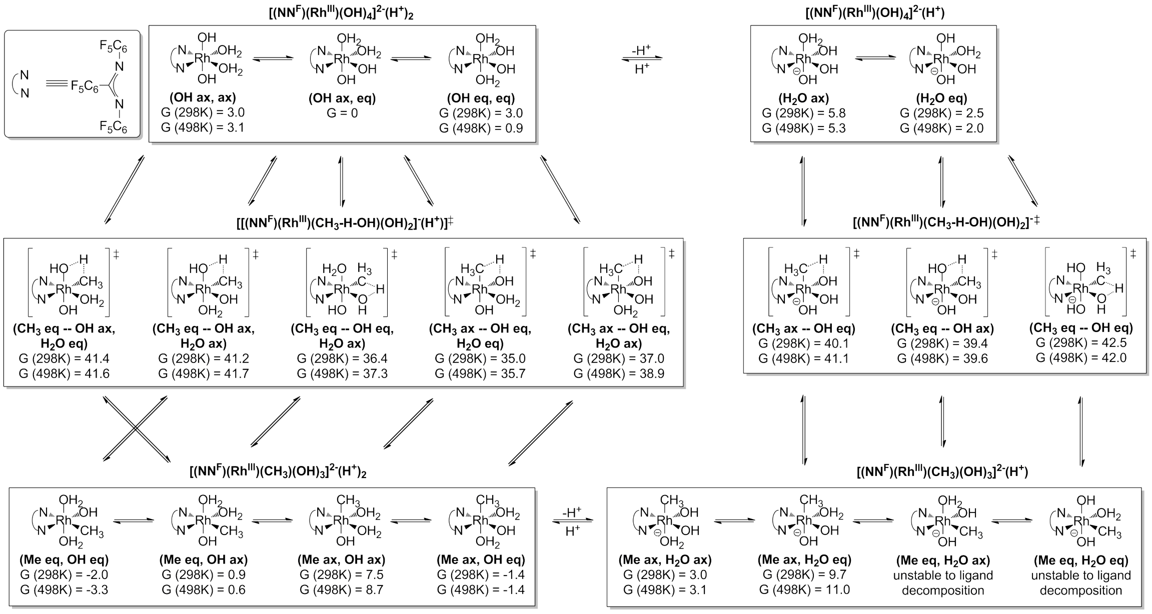

Scheme 3.5. Transition states for the activation of methane using $Rh(NN^F)$ complexes in water. Chart is meant to be read from top to bottom; the left side contains the pathway through neutral species and the right side through anionic species. All free energies are in kcal/mol and referenced to the lowest inorganic Rh^{III} state.

Following the activation of methane, the other transition state that needed to be calculated was for the functionalization of the rhodium-methyl bond. We investigated the functionalization through

Figure 3.4. Rh(NN^F) in water transition state structures. (a) methane activation: Rh1-C66 2.296 Å, C66-H65 1.383 Å, H65-O5 1.271 Å, Rh1-C66-H65 55.587°, C66-H65-O5 161.845°. (b) Rh(III-I) S_N2 attack: Rh1-C64 2.698 Å, C64-O67 1.803 Å, O67-H68 1.043 Å, H68-O47 1.516 Å, O47-H53 1.001 Å, H53-O5 1.718 Å, Rh1-C60-O65 148.135°, Rh1-O54 3.265 Å. (c) Rh(III-II) S_R2 attack: Rh1-C65 2.371 ÅC65-O68 2.010 Å, Rh1-O55 2.228 Å, Rh1-C65-O68 164.320°, C65-Rh1-O55 169.736°. (d) Rh(III-IV-II) S_N2 attack: Rh1-C64 2.526 Å, C64-O67 1.930 Å, O67-H68 1.033 Å, H68-O46 1.503 Å, O46-H51 1.008 Å, H51-O47 1.594 Å, O47-H3 0.981 Å, H3-O5 1.901 Å, Rh1-O54 2.255 Å, Rh1-C64-O67 171.136°, C64-Rh1-O54 167.491°.

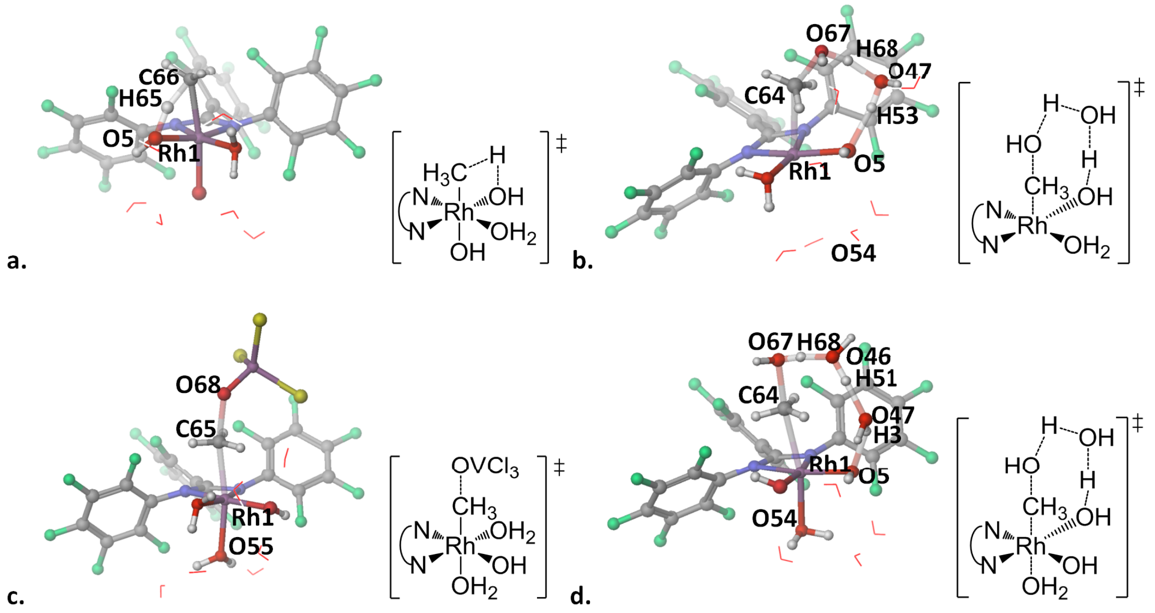

the III-I, III-II, and III-IV-II routes (Schemes 3.6, 3.7, and 3.8, respectively). For each route, we restricted our investigation to activations from rhodium species with axial methyl groups, since (as in the TFAH case) the axial isomer is preferentially formed during the activation step.

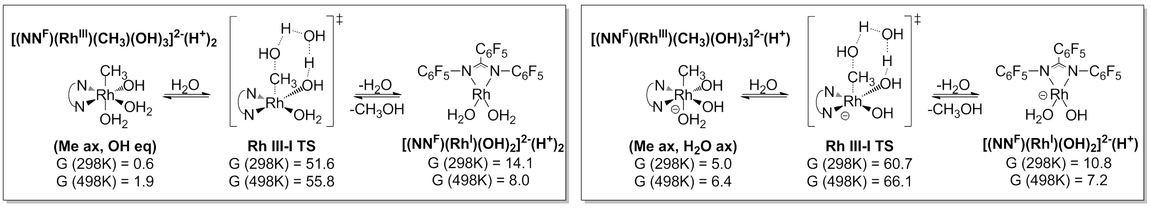

Scheme 3.6. Transition states for the III-I functionalization pathway *via* S_N2 attack in water. The left side is the pathway through neutral species and the right side through anionic species. All free energies are in kcal/mol and referenced to the resting state, $[(NN^F)Rh^{III}(Me_{eq})(OH)_3]^{2-}(H^+_{ax})_2$.

For the III-I route, we required an aqua ligand to be the leaving group *trans* to the methyl, limiting us to only two possible transition states: a neutral transition complex (Scheme 3.6, left) and an anionic complex (Scheme 3.6, right). Although the neutral transition state (Figure 3.4b) is somewhat lower in energy, we found that in both cases the activation energy for this pathway is prohibitively high.

For the III-II route (Scheme 3.7), we no longer needed require the leaving group *trans* to the Rh^{III}-methyl to be an aqua ligand. Hence we performed calculations on four different potential transition states, starting with two isomers of neutral $[(NN^F)Rh^{III}(Me_{ax})(OH)_3]^{2-}(H^+)_2$ (Scheme 3.7, upper left) and two isomers of anionic $[(NN^F)Rh^{III}(Me_{ax})(OH)_3]^{2-}(H^+)$ (Scheme 3.7, upper right). We found that this S_R2 pathway was even more facile, with all barriers in the 30s (Scheme 3.7, middle) and the lowest barrier being 31.7 kcal/mol for $OVCl_3$ attack on a neutral species with an axial methyl ligand, which is shown in detail in Figure 3.4c.

For the III-IV-II route (Scheme 3.8), a good leaving group *trans* to the Rh^{III}-methyl once again became important. Hence, we were limited to only investigating one possible transition state, shown in detail in Figure 3.4d. We found the activation energy for this process to be approximately equal to that of the methane activation step.

Hence, we conclude that for the $Rh(NN^F)$ catalytic system in water, both III-IV-II S_N2 and III-II S_R2 are viable pathways for functionalization, whereas the III-I S_N2 pathway is still too high in energy. This is similar to the case in TFAH, except that the relative ease of activation *vis-à-vis* functionalization has now been reversed.

3.4.4 The Rh(ONN^x) family of complexes in TFAH

Schemes 3.9, 3.10, and 3.11 depict the catalytic cycle for the activation and functionalization of methane using Rh(ONN), $Rh(ONN^F)$, and $Rh(ONN^{NMe_2})$ complexes in TFAH, respectively. In all

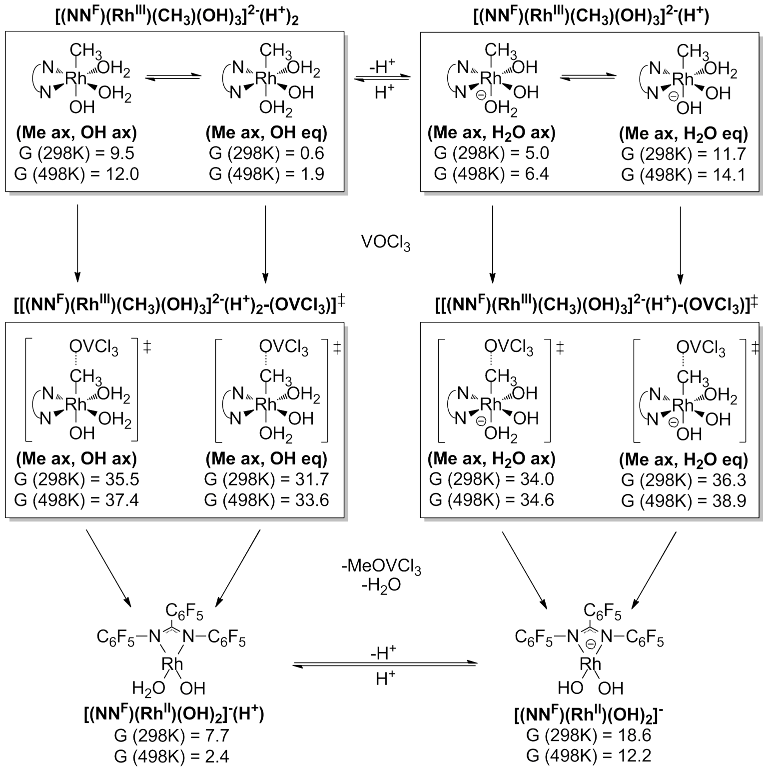

Scheme 3.7. Transition states for the III-II functionalization pathway *via* S_R2 attack in water. This chart is meant to be read from top to bottom; the left side contains the pathway through neutral species and the right side through anionic species. All free energies are in kcal/mol and referenced to the resting state, $[(NN^F)Rh^{III}(Me_{eq})(OH)_3]^{2-}(H^+_{ax})_2$.

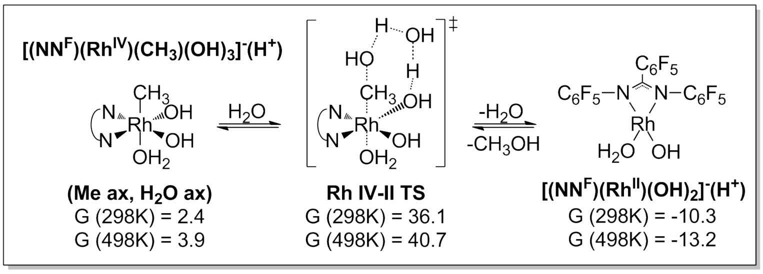

Scheme 3.8. Transition state for the III-IV-II functionalization pathway *via* S_N2 attack in water. All free energies are in kcal/mol and referenced to the resting state, $[(NN^F)Rh^{III}(Me_{eq})(OH)_3]^{2-}(H^+_{ax})_2$.

cases, the resting state contains an axial TFAH ligand and equatorial TFA ligands, but the activation transition state which involves an axial methyl group is slightly lower in energy than the transition state which involves an equatorial methyl group. The methane activation energy for Rh(ONN) is 37.2 kcal/mol at 298 K, which is somewhat too high for promising catalysis. Switching to Rh(ONN^{F}) decreases this activation energy slightly to 35.8 kcal/mol, whereas using Rh(ONN^{NMe_2}) raises it to 38.7 kcal/mol.

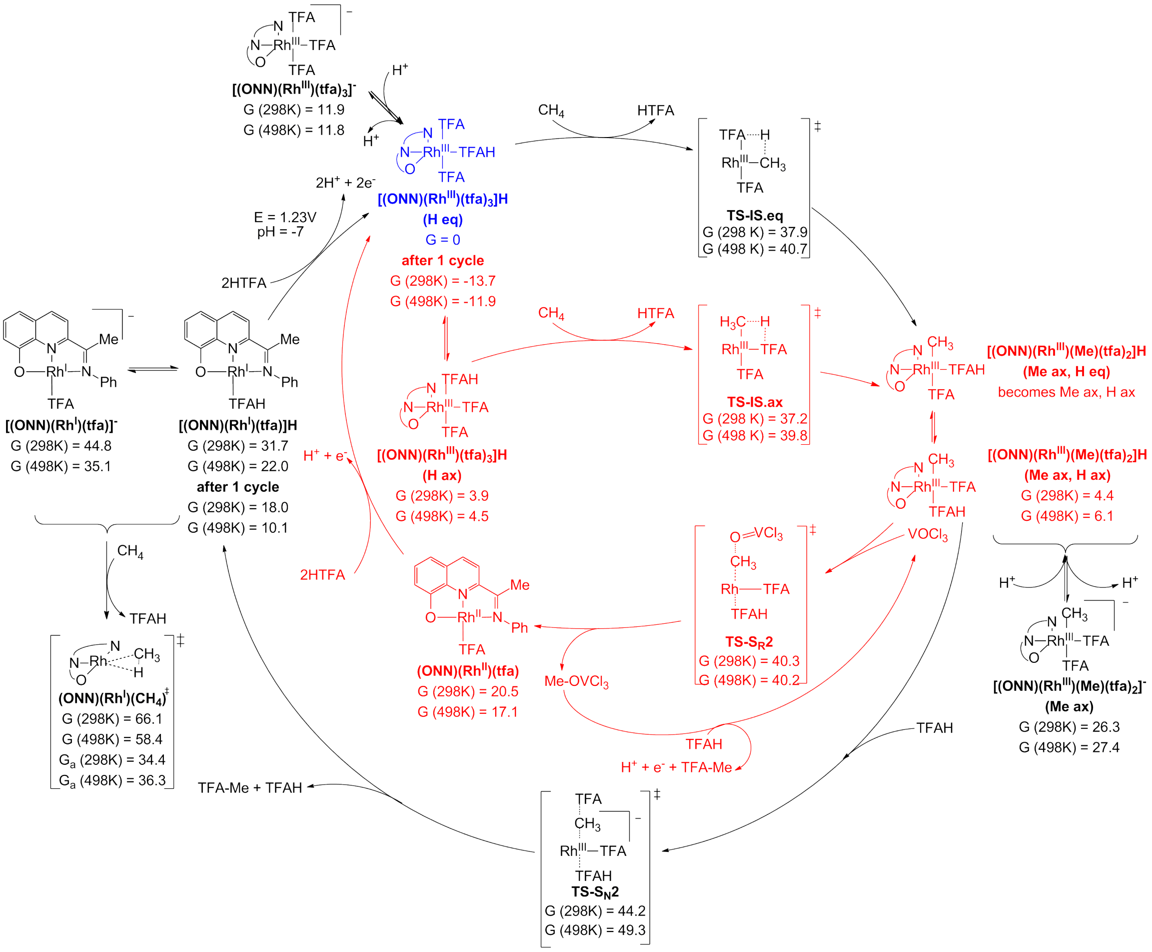

Scheme 3.9. Catalytic cycle for the activation and functionalization of methane using Rh(ONN) complexes in TFAH. Blue denotes the resting state and red the most favored pathway. All free energies are in kcal/mol.

The Rh^{III}(ONN^{x})–Me species investigated have a methyl group axial to the (ONN^{x}) plane; any isomer with an equatorial methyl group would likely be less stable due to the *trans* effect of the (ONN^{x})'s quinoline nitrogen. The Rh^{III}(ONN^{x})–Me species are slightly endergonic relative to their respective resting states.

In all cases, the III-II S$_R$2 pathway is favored over the III-I S$_N$2 pathway. For Rh(ONN) the S$_R$2 barrier is 40.3 kcal/mol at 298 K; this decreases to 39.2 kcal/mol for Rh(ONN^{F}) but increases

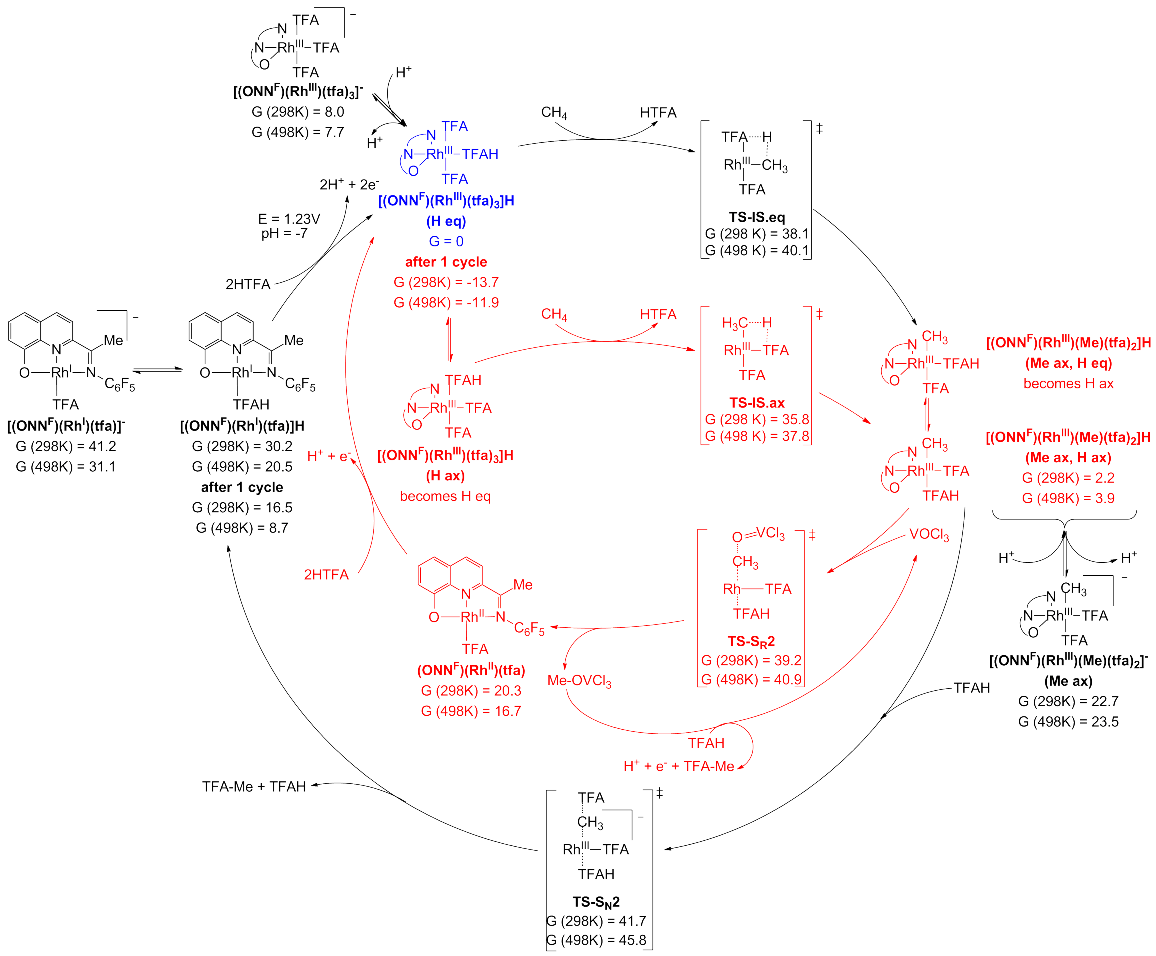

Scheme 3.10. Catalytic cycle for the activation and functionalization of methane using Rh(ONN^F) complexes in TFAH. Blue denotes the resting state and red the most favored pathway. All free energies are in kcal/mol.

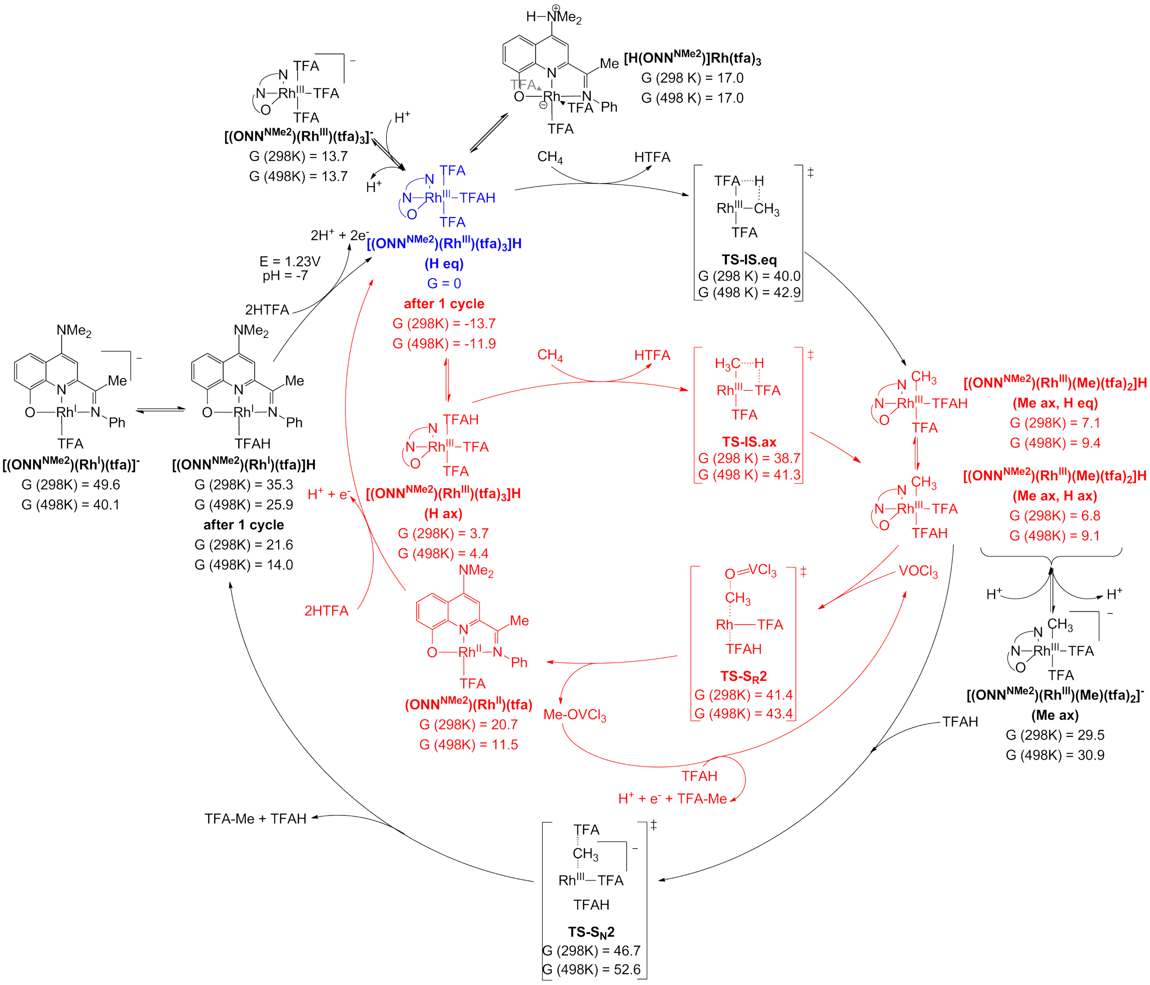

Scheme 3.11. Catalytic cycle for the activation and functionalization of methane using Rh(ONN$^{\mathrm{NMe_2}}$) complexes in TFAH. Blue denotes the resting state and red the most favored pathway. All free energies are in kcal/mol.

to 41.4 kcal/mol for Rh(ONN$^{\mathrm{NMe_2}}$). The resultant Rh$^{\mathrm{III}}$(ONN^{x}) species were all approximately the same (20.5, 20.3, and 20.7 kcal/mol, respectively) in energy relative to their resting states.

3.4.5 The Rh(DPMS) and Rh(DPES) complexes in TFAH

Scheme 3.12 shows the catalytic cycle for the activation and functionalization of methane using Rh(DPMS) complexes in TFAH, with the latter *via* the Rh(III-I), Rh(III-II), and Rh(III-IV-II) pathways. While there is a relatively accessible activation barrier of 33.9 kcal/mol at 298 K, it differs from the activation transition states of the NN^{x} and ONN^{x} families in that it forms a methyl complex with the methyl group equatorial to the N−Rh−N plane. Interconvertibility with the lower-energy axial methyl complex is assumed given the lability of the sulfonate moiety and the TFAH ligands. Unfortunately, the lowest functionalization barrier found was 41.0 kcal/mol at 298 K for the III-II pathway, which is too high.

The analogous catalytic cycle for Rh(DPES) complexes in TFAH is shown in Scheme 3.13. The energy profile is very similar to that of the Rh(DPMS) complexes; however, the transition states found are typically several kcal/mol higher than their Rh(DPMS) counterparts. This may be due to the extra methyl group rendering the overall ligand more electron donating, destabilizing the formation of a Rh−Me bond and decreasing its electrophilicity for functionalization.

We also investigated Rh$^{\mathrm{I}}$(DPMS) species, the results of which are shown in Scheme 3.14. The energy profile appears to be much more favorable, with the highest barrier being the oxidative addition of methane at 26.4 kcal/mol at 298 K. However, under reaction conditions one might expect the oxidative addition of methane by Rh$^{\mathrm{I}}$(DPMS) to be outcompeted by Rh$^{\mathrm{I}}$(DPMS)'s oxidation to a Rh$^{\mathrm{III}}$(DPMS) species, which according to Scheme 3.12 is downhill by 33.0 kcal/mol at 298 K. Therefore, the I-III pathway was not considered to be viable.

3.4.6 The Rh(PN) complexes in TFAH

Scheme 3.15 shows the catalytic cycle for the activation and functionalization of methane using Rh(PN) complexes in TFAH, with the latter *via* the Rh(III-I) and Rh(III-II) pathways. Unfortunately, it appears that the functionalization barriers are too high for effective catalysis with this ligand: the lowest III-I $\mathrm{S_N2}$ barrier is 38.0 kcal/mol at 298 K and the lowest III-II $\mathrm{S_R2}$ barrier is 47.7 kcal/mol. Taking into account the additional fact that the activation transition state to produce an axial methyl species is 40.1 kcal/mol high, we conclude that Rh$^{\mathrm{III}}$(PN) is not likely to be an effective catalyst for methane oxidation.

We also investigated Rh$^{\mathrm{I}}$(PN) species, the results of which are shown in Scheme 3.16. As in the case of the Rh(DPMS) complexes, oxidative addition of methane by Rh$^{\mathrm{I}}$(PN) appears to be more facile, with a barrier of 28.1 kcal/mol at 298 K. Unfortunately, the resultant Rh$^{\mathrm{III}}$(PN)(H)(Me)

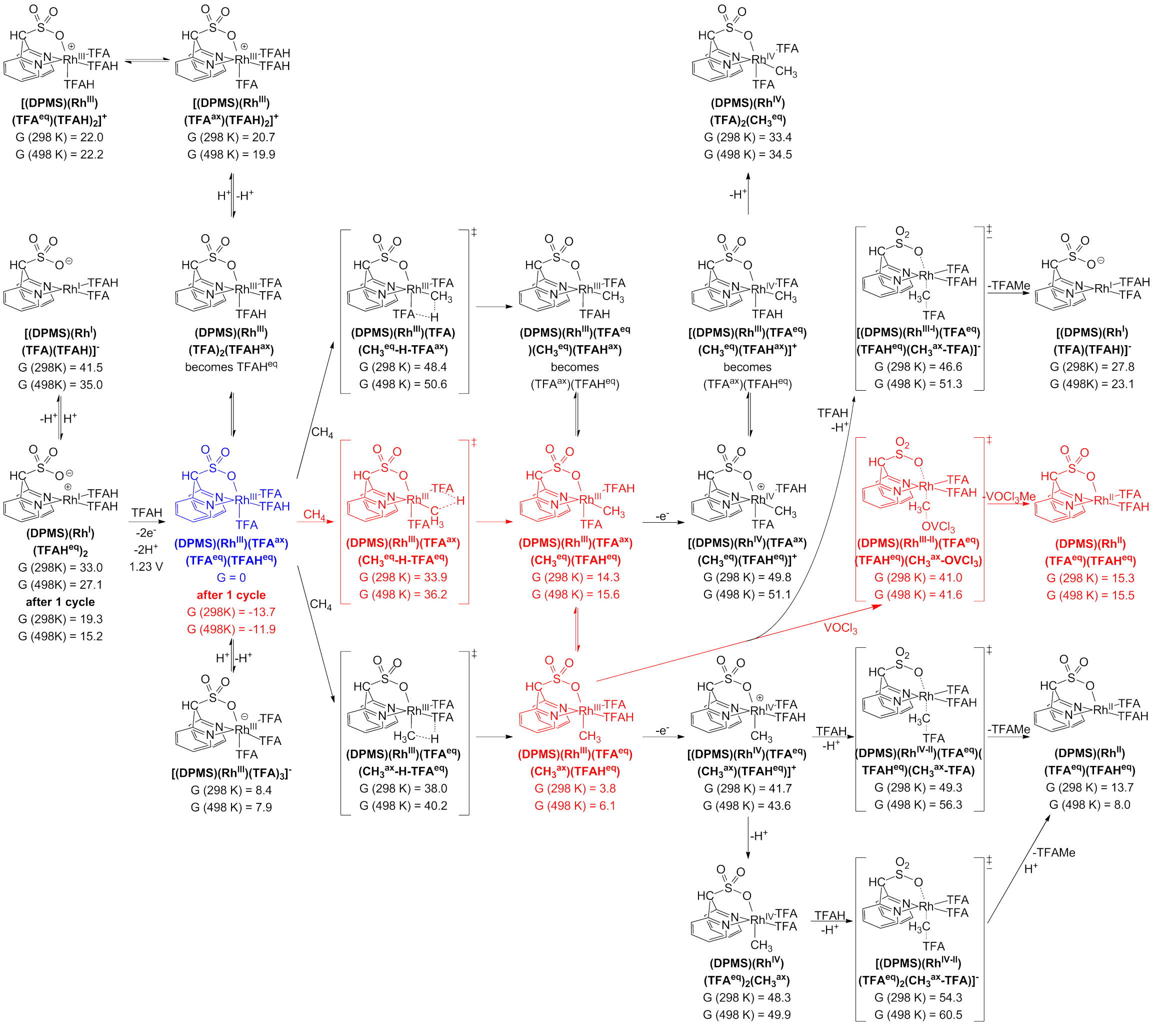

Scheme 3.12. The activation and functionalization of methane using Rh(DPMS) complexes in TFAH, *via* the Rh(III-I), Rh(III-II), and Rh(III-IV-II) pathways. Blue denotes the resting state and red the most favored pathway. All free energies are in kcal/mol.

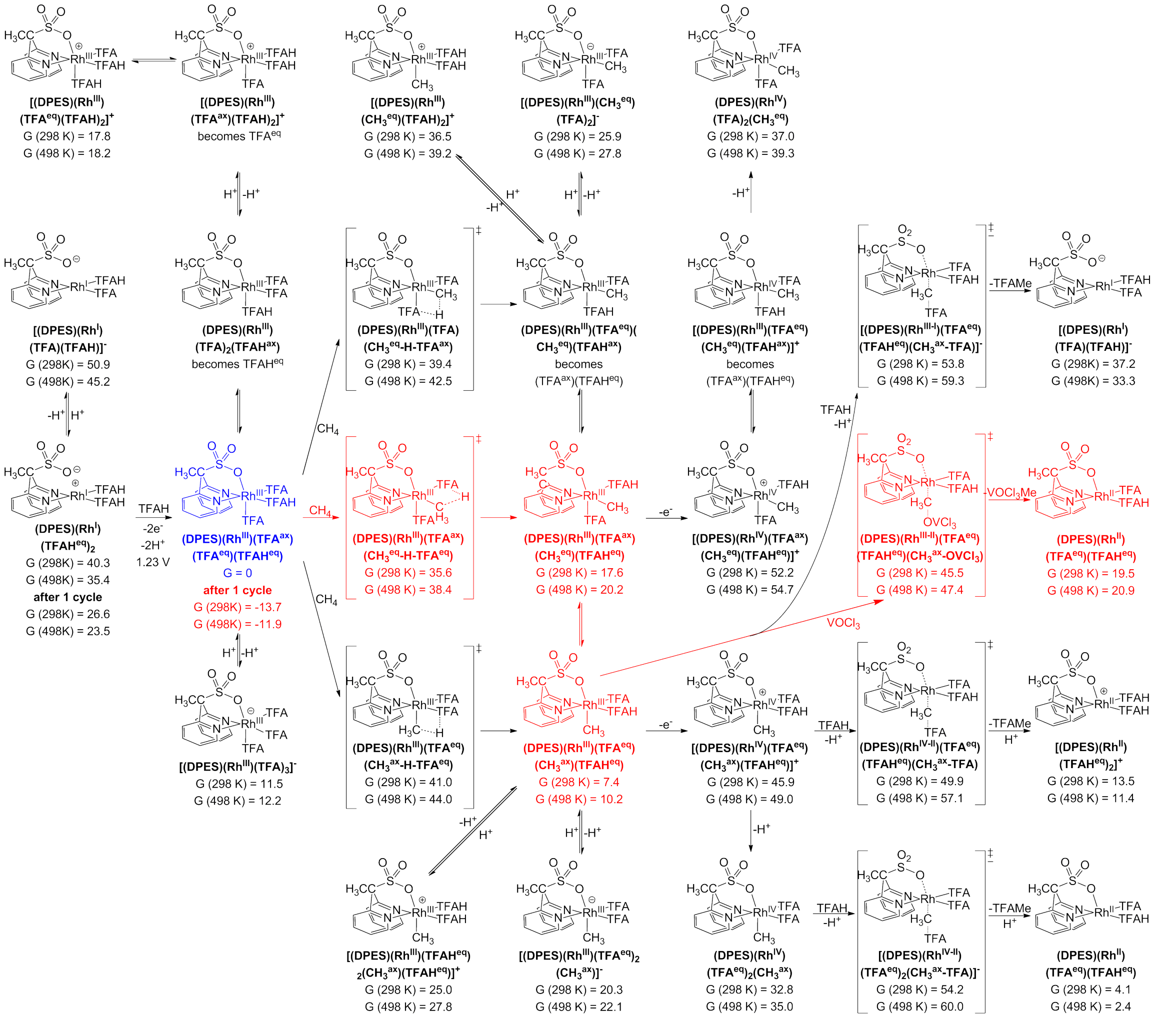

Scheme 3.13. The activation and functionalization of methane using Rh(DPES) complexes in TFAH, *via* the Rh(III-I), Rh(III-II), and Rh(III-IV-II) pathways. Blue denotes the resting state and red the most favored pathway. All free energies are in kcal/mol.

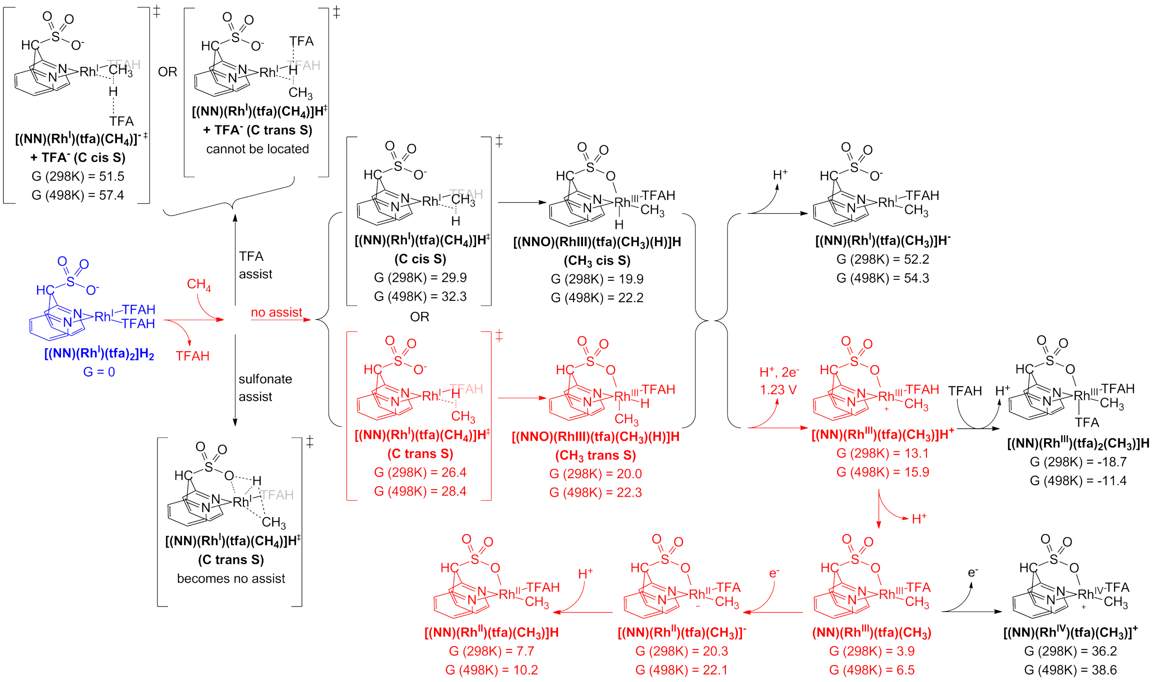

Scheme 3.14. Catalytic cycle for the activation and functionalization of methane using Rh(DPMS) complexes in TFAH, *via* the Rh(I-III) pathway. Blue denotes the resting state and red the most favored pathway. All free energies are in kcal/mol.

species are all significantly thermodynamically uphill (at least 22.0 kcal/mol at 298 K). Furthermore, as in the case of the Rh(DPMS) complexes, under reaction conditions one might expect the oxidative addition of methane by Rh^I(PN) to be outcompeted by Rh^I(PN)'s oxidation to a Rh^{III}(PN) species, which according to Scheme 3.15 is downhill by 23.7 kcal/mol at 298 K. Therefore, the I-III pathway was not further pursued.

3.4.7 The Rh(bisq^x) family of complexes in TFAH

Due to the large in-TFAH Rh−Me functionalization barriers encountered in the other ligands so far (Table 3.2), we designed the bis(quinolinyl) benzene (bisq^x) family of ligands (Figure 3.1) in the hopes of finding more facile S_N2 and S_R2 pathways. These ligands would be expected to be coordinated to rhodium in a *fac*-L_3 manner, with a weak η^2-benzene interaction axial to the N−Rh−N plane. A methyl group would then be expected to be coordinated axial to the N−Rh−N plane as well, due to the weaker *trans* effect of the benzene ring as opposed to the nitrogen donors. The η^2-benzene interaction is also expected to be a better leaving group than TFA/TFAH, thereby lowering both the barrier and thermodynamics of functionalization. Beyond the base (bisq) ligand itself, we also investigated the di- and tetrafluorinated analogues (bisq^{F_2}) and (bisq^{F_4}), and the di- and tetramethylated analogues (bisq^{Me_2}) and (bisq^{Me_4}), to see how changing the electronics of the ligand

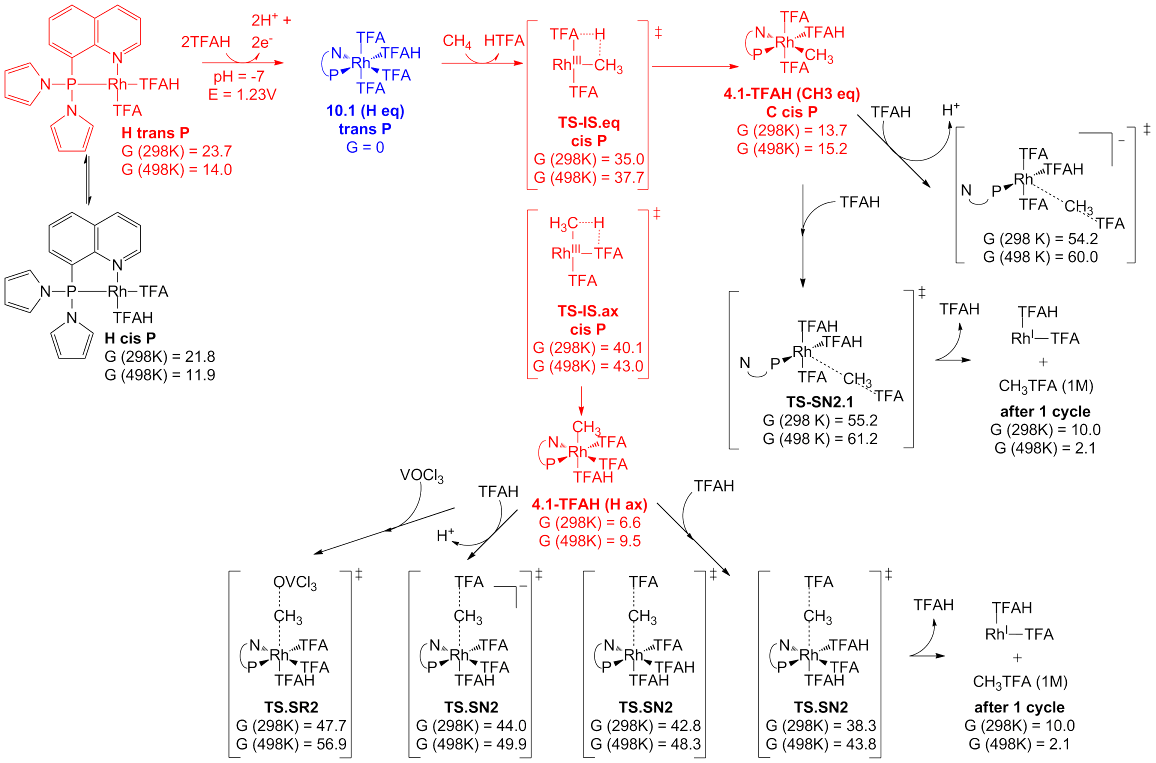

Scheme 3.15. Catalytic cycle for the activation and functionalization of methane using Rh(PN) complexes in TFAH, *via* the Rh(III-I) and Rh(III-II) pathways. Blue denotes the resting state and red the most favored pathway. All free energies are in kcal/mol.

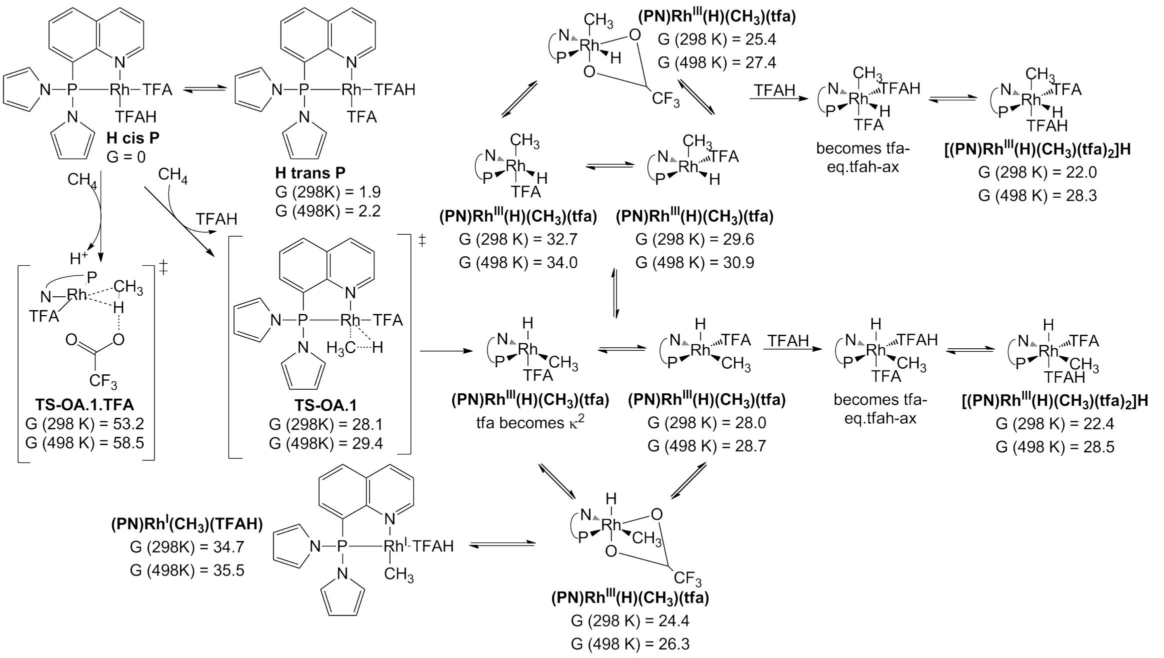

Scheme 3.16. Catalytic cycle for the activation and functionalization of methane using Rh(PN) complexes in TFAH, *via* the Rh(I-III) pathway. Blue denotes the resting state and red the most favored pathway. All free energies are in kcal/mol.

might change its associated transition state barriers.

Scheme 3.17 shows the ground states of the various $\text{Rh}^{\text{III}}(\text{bisq}^{x})$ species: the neutral $\text{Rh}^{\text{III}}(\text{bisq}^{x})$-$(\text{TFA})_3$, the protonated $[\text{Rh}^{\text{III}}(\text{bisq}^{x})(\text{TFA})_2(\text{TFAH})]^+$ and $[\text{Rh}^{\text{III}}(\text{bisq}^{x})(\text{TFA})_2)]^+$, and their relative free energies. The first point to note is that, since the (bisq^{x}) ligands are L_3, activation of methane requires first the protonation of a TFA ligand followed by its removal as TFAH to form an open coordination site. As Scheme 3.17 shows, as we increase the electron-withdrawing groups on (bisq^{x}), replacing Me with H and H with F, the resultant decrease in electron donation to the central Rh decreases the basicity of the attached TFA ligands and increases the energy of their protonated forms. The second and related point to note is that the true resting state is not consistent for all (bisq^{x}) species: the more electron-rich ligands $(\text{bisq}^{\text{Me}_2})$ and $(\text{bisq}^{\text{Me}_4})$ have positively-charged resting states, the base ligand (bisq) has both the neutral and a protonated species in even equilibrium, while the less electron-rich ligands $(\text{bisq}^{\text{F}_2})$ and $(\text{bisq}^{\text{F}_4})$ prefer to be neutral. However, the energies of all species have been referenced to neutral $\text{Rh}^{\text{III}}(\text{bisq}^{x})(\text{TFA})_3$ for consistency. The final point to note is that the specific protonated resting state for the more electron-rich ligands $(\text{bisq}^{\text{Me}_2})$ and $(\text{bisq}^{\text{Me}_4})$ depends on temperature: at 298 K $[\text{Rh}^{\text{III}}(\text{bisq}^{\text{Me}_x})(\text{TFA}_{\text{ax}})(\text{TFAH}_{\text{eq}}\cdots\text{TFA}_{\text{eq}})]^+$ is favored, but at 498 K it is more advantageous to dissociate the TFAH and have $[\text{Rh}^{\text{III}}(\text{bisq}^{\text{Me}_x})(\kappa^1{-}\text{TFA}_{\text{eq}})(\kappa^2{-}\text{TFA}_{\text{ax, eq}})]^+$ instead.

Scheme 3.18 shows the three potential methane activation transition states that may result

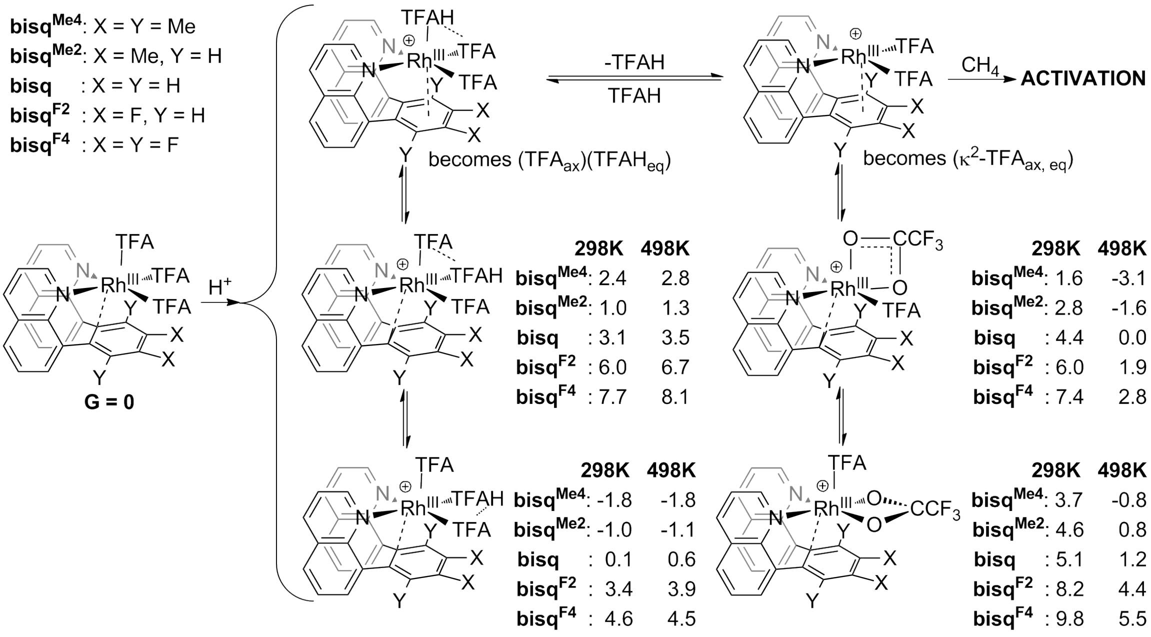

Scheme 3.17. The inorganic $\mathrm{Rh^{III}(bisq^{x})(TFA)_3}$ species and its protonated analogues $\mathrm{[Rh^{III}(bisq^{x})(TFA)_2(TFAH)]^+}$ and $\mathrm{[Rh^{III}(bisq^{x})(TFA)_2)]^+}$, along with their relative energies in TFAH. Both protonation and TFAH removal are necessary before methane activation can take place. All free energies are in kcal/mol and referenced to the corresponding $\mathrm{Rh^{III}(bisq^{x})(TFA)_3}$ species.

depending on the CH_4 molecule's approach towards the $\mathrm{[Rh^{III}(bisq^{x})(TFA)_2)]^+}$'s open coordination site. The top transition state shows the result of a methane approach to an axial open coordination site, whereas the other two show the result of an equatorial approach, with either the axial or equatorial TFA ligand gaining the methane's proton. The axial approach results in a $\mathrm{[Rh^{III}{-}Me_{ax}]^+}$ species, whereas the equatorial approaches result in $\mathrm{[Rh^{III}{-}Me_{eq}]^+}$ species, all of which may be deprotonated to form their neutral analogues. Further oxidation to $\mathrm{Rh^{IV}}$ species is quite uphill; hence the III-IV-II functionalization pathway was not investigated for these rhodium-ligand complexes.

It should be noted that regardless of the specific $\mathrm{(bisq^{x})}$ ligand, the lowest energy methane activation transition state is $\mathrm{[Rh^{III}(bisq^{x})(TFA_{ax})(Me_{eq}\cdots H\cdots TFA_{eq})]^{+\ddagger}}$, which involves an equatorial approach for the methane and results in the methyl complex $\mathrm{[Rh^{III}(bisq^{x})(TFA_{ax})(Me_{eq})(TFAH_{eq})]^+}$. However, both the neutral and protonated $\mathrm{Rh^{III}{-}Me_{ax}}$ species are lower in energy than their equatorial counterparts. We assume that interconversion between the $\mathrm{Rh^{III}{-}Me_{eq}}$ and $\mathrm{Rh^{III}{-}Me_{ax}}$ is facile due to the lability of the TFAH and η^2-benzene ligands.

Upon examination of the methane activation transition state energies, it appears that the general trend is that increasing the electron-donating nature of groups on the (bisq) ligand appears to favor lower barriers. This is opposite to that observed in the other ligand families, in which less electron-donating ligands are preferred. However, a comparison of the energies of $\mathrm{[Rh^{III}(bisq^{x})(TFA)\text{-}(Me\cdots H\cdots TFA)]^{+\ddagger}}$ transition states with that of their protonated $\mathrm{[Rh^{III}(bisq^{x})(TFA)_2(TFAH)]^+}$

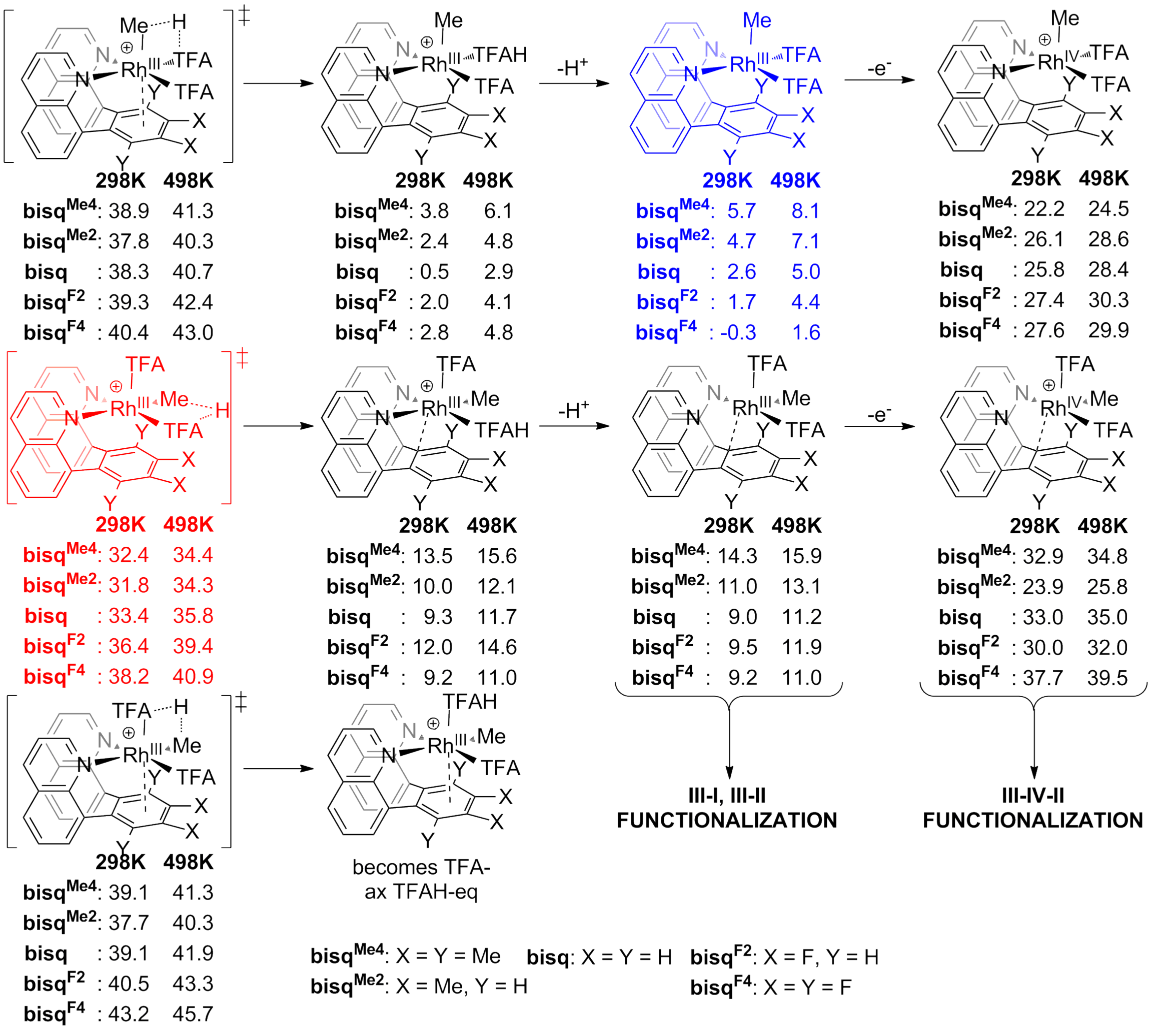

Scheme 3.18. The various methane activation transition states $[\mathrm{Rh^{III}}(\mathrm{bisq}^{x})(\mathrm{TFA})(\mathrm{Me}\cdots\mathrm{H}\cdots\mathrm{TFA})]^{+\ddagger}$ and their resultant $[\mathrm{Rh^{III}}(\mathrm{bisq}^{x})(\mathrm{TFA})(\mathrm{Me})(\mathrm{TFAH})]^{+}$ products. Ensuing deprotation (in preparation for III-I and III-II functionalization) and oxidation (in preparation for III-IV-II functionalization) are also depicted. Blue denotes the most favored Rh−Me intermediate and red the most favored activation transition state. All free energies are in kcal/mol and referenced to the corresponding $\mathrm{Rh^{III}}(\mathrm{bisq}^{x})(\mathrm{TFA})_3$ species.

precursors (Scheme 3.17) shows that the decreased activation barriers for more electron-donating ligands is simply due to the decreased energy of protonation of the inorganic $\mathrm{Rh^{III}(bisq^{x})(TFA)_3}$ precursors. It should also be noted that for $\mathrm{(bisq^{Me_2})}$ and $\mathrm{(bisq^{Me_4})}$, the energies shown in Scheme 3.18 are not the full transition barriers, since they are not referenced to the ground states of those rhodium-ligand complexes. The true barriers are recorded in Table 3.2.

An examination of the energies of the lowest Rh−Me intermediate for each $\mathrm{(bisq^{x})}$ ligand (Scheme 3.18, blue) shows that the relative energy decreases as the electron-withdrawing nature of groups on the (bisq) ligand is increased. This is easily explained by noting that a decrease in the electron-donating power of the (bisq) ligand is expected to increase the rhodium atom's electrophilicity, and thus increase the strength of its bond with the methyl group. Indeed, for $\mathrm{(bisq}^{F_4})$ the Rh−Me species is slightly lower (by 0.3 kcal/mol) in energy than its $\mathrm{Rh^{III}(bisq^{x})(TFA)_3}$ precursor at 298 K, and is the true resting state. However, this does not change the overall methane activation barrier.

The III-I $\mathrm{S_N2}$ and III-II $\mathrm{S_R2}$ functionalization pathways were investigated by searching for transition states resulting from $\mathrm{TFA^-}$/TFAH or $\mathrm{OVCl_3}$ attack on each Rh−Me species, axial and equatorial, neutral and positively charged; for all five $\mathrm{(bisq^{x})}$ ligands. A total of 65 transition state structures were analyzed.

Figure 3.5 shows the functionalization transition states for $\mathrm{S_N2}$ attack by $\mathrm{TFA^-}$/TFAH on various Rh−Me intermediates. Both $\mathrm{H^+}$ pre-protonation followed by $\mathrm{TFA^-}$ attack and concerted TFAH attack/deprotonation transition states were investigated. The lowest energy $\mathrm{S_N2}$ functionalization barrier was found to arise from the attack of a $\mathrm{TFA^-}$ ion on a protonated $\mathrm{Rh{-}Me_{ax}}$ species. Not surprisingly, lower barriers were found for $\mathrm{Rh^{III}(bisq^{x})}$ complexes with less electron-donating ligands. The energies are overall significantly lower than those found with other ligand families, thus confirming our initial hypothesis that a weak η^2-benzene coordinated *trans* to the methyl would facilitate $\mathrm{S_N2}$ attack. Indeed, barriers of 34.1 kcal/mol and lower at 298 K are found for (bisq) and its fluorinated analogues, thereby establishing the viability of the $\mathrm{Rh^{III}(bisq^{x})}$ family of complexes as potentially effective catalysts.

Figure 3.6 shows the functionalization transition states for $\mathrm{S_R2}$ attack by $\mathrm{OVCl_3}$ on both neutral $\mathrm{Rh^{III}(bisq^{x})(Me)(TFA)_2}$ and protonated $\mathrm{[Rh^{III}(bisq^{x})(Me)(TFA)(TFAH)]^+}$ species, with both axial and equatorial methyl conformations. In most cases the lowest energy $\mathrm{S_R2}$ functionalization barrier was found to arise from the attack of a $\mathrm{OVCl_3}$ molecule on a neutral $\mathrm{Rh{-}Me_{ax}}$ species (the lone exception is $\mathrm{(bisq^{Me4})}$, which prefers a protonated transition state). As in the III-I $\mathrm{S_N2}$ case, lower barriers were found for $\mathrm{Rh^{III}(bisq^{x})}$ complexes with less electron-donating ligands, and overall the barriers were reduced compared to those of other ligand families; although the effect is not as pronounced as for the $\mathrm{S_N2}$ case, and the tetrafluorinated $\mathrm{(bisq^{F4})}$ version is an outlier. Barriers of 33.4 kcal/mol and lower at 298 K are found for (bisq) and its fluorinated analogues, thereby establishing

Figure 3.5. The various Rh^{III}(bisq^x)(Me) functionalization transition states for the III-I S$_N$2 pathway. All transition states resulting from TFA$^-$/TFAH attack on each Rh−Me species, axial and equatorial, neutral and positively charged, are shown. The lowest transition state for each (bisq^x) ligand is shown in red. All free energies are in kcal/mol and referenced to the corresponding Rh^{III}(bisq^x)(TFA)$_3$ species.

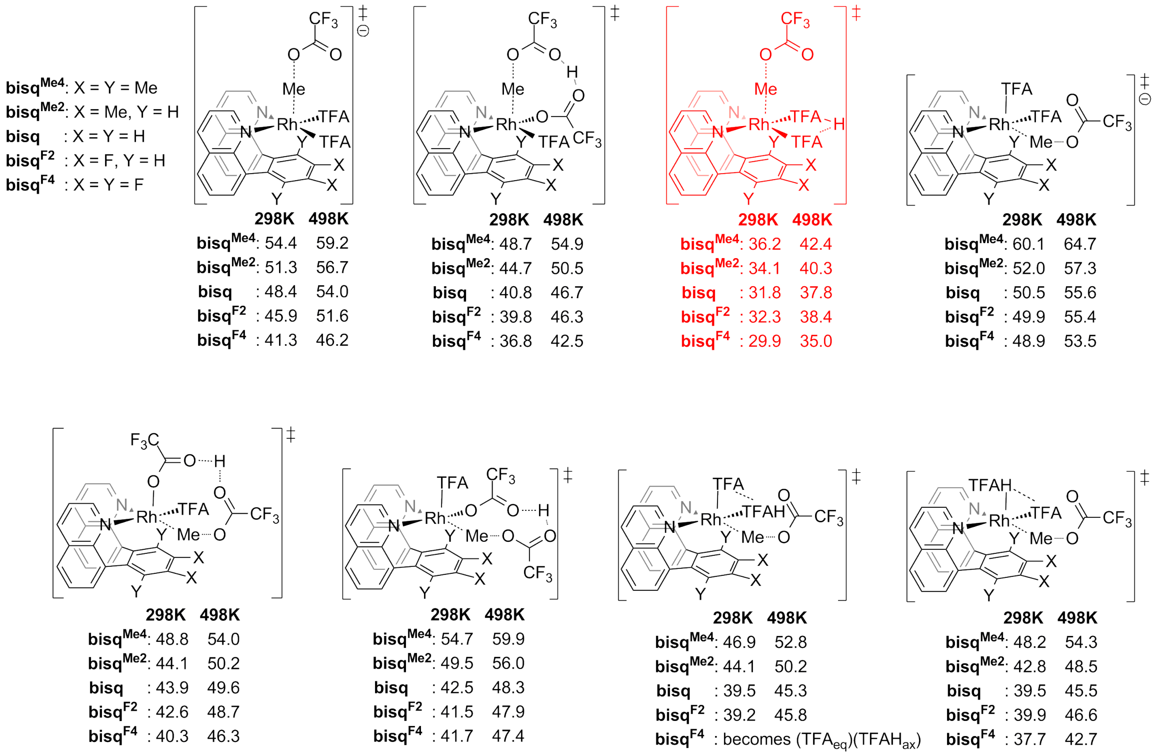

bisq^{Me4}: X = Y = Me
bisq^{Me2}: X = Me, Y = H
bisq : X = Y = H
bisq^{F2} : X = F, Y = H
bisq^{F4} : X = Y = F

	298K	**498K**
bisq^{Me4}	54.4	59.2
bisq^{Me2}	51.3	56.7
bisq	48.4	54.0
bisq^{F2}	45.9	51.6
bisq^{F4}	41.3	46.2

	298K	**498K**
bisq^{Me4}	48.7	54.9
bisq^{Me2}	44.7	50.5
bisq	40.8	46.7
bisq^{F2}	39.8	46.3
bisq^{F4}	36.8	42.5

	298K	**498K**
bisq^{Me4}	36.2	42.4
bisq^{Me2}	34.1	40.3
bisq	31.8	37.8
bisq^{F2}	32.3	38.4
bisq^{F4}	29.9	35.0

	298K	**498K**
bisq^{Me4}	60.1	64.7
bisq^{Me2}	52.0	57.3
bisq	50.5	55.6
bisq^{F2}	49.9	55.4
bisq^{F4}	48.9	53.5

	298K	**498K**
bisq^{Me4}	48.8	54.0
bisq^{Me2}	44.1	50.2
bisq	43.9	49.6
bisq^{F2}	42.6	48.7
bisq^{F4}	40.3	46.3

	298K	**498K**
bisq^{Me4}	54.7	59.9
bisq^{Me2}	49.5	56.0
bisq	42.5	48.3
bisq^{F2}	41.5	47.9
bisq^{F4}	41.7	47.4

	298K	**498K**
bisq^{Me4}	46.9	52.8
bisq^{Me2}	44.1	50.2
bisq	39.5	45.3
bisq^{F2}	39.2	45.8
bisq^{F4}	becomes (TFA$_{eq}$)(TFAH$_{ax}$)	

	298K	**498K**
bisq^{Me4}	48.2	54.3
bisq^{Me2}	42.8	48.5
bisq	39.5	45.5
bisq^{F2}	39.9	46.6
bisq^{F4}	37.7	42.7

the viability of the III-II pathway as well as the III-I pathway for methyl functionalization of the $\mathrm{Rh^{III}}(\mathrm{bisq}^{x})$ family of complexes.

Figure 3.6. The various $\mathrm{Rh^{III}}(\mathrm{bisq}^{x})(\mathrm{Me})$ functionalization transition states for the III-II $\mathrm{S_R}2$ pathway. All transition states resulting from $\mathrm{OVCl_3}$ attack on each Rh−Me species, axial and equatorial, neutral and positively charged, are shown. The lowest transition state for each (bisq^{x}) ligand is shown in red. All free energies are in kcal/mol and referenced to the corresponding $\mathrm{Rh^{III}}(\mathrm{bisq}^{x})(\mathrm{TFA})_3$ species.

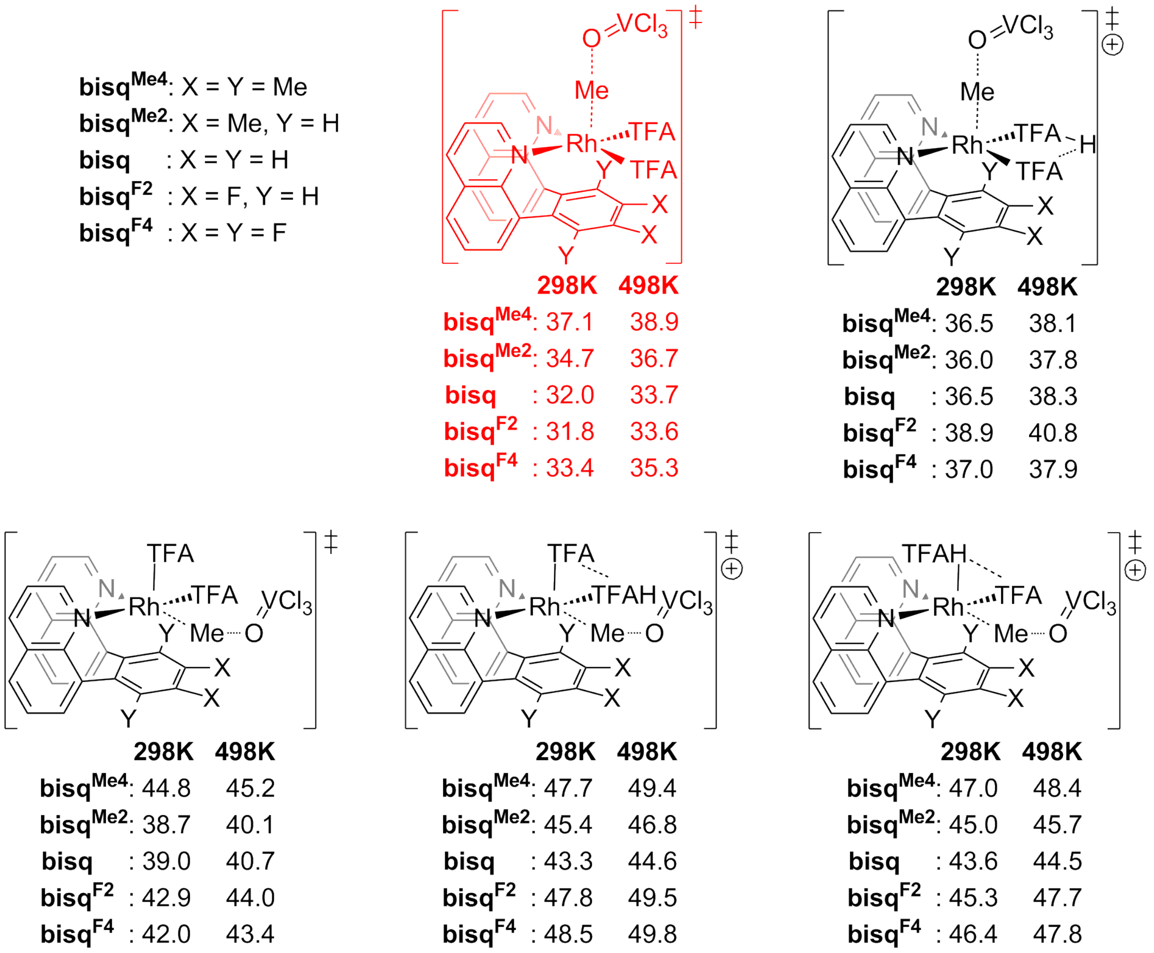

Scheme 3.19 shows the remainder of the catalytic cycle after either III-I or III-II functionalization, and compares the two functionalization processes. For the III-I pathway, $\mathrm{S_N}2$ attack by $\mathrm{TFA^-}$/TFAH results in the formation of the Me−TFA product and $\mathrm{Rh^{I}}(\mathrm{bisq}^{x})(\mathrm{TFA})(\mathrm{TFAH})$, which is reoxidized to the starting complex $\mathrm{Rh^{III}}(\mathrm{bisq}^{x})(\mathrm{TFA})_3$. For the III-II pathway, $\mathrm{S_R}2$ attack by $\mathrm{OVCl_3}$ results in the formation of $\mathrm{Me{-}OVCl_3}$ and $\mathrm{Rh^{II}}(\mathrm{bisq}^{x})(\mathrm{TFA})(\mathrm{TFAH})$, which are also reoxidized to the starting complex $\mathrm{Rh^{III}}(\mathrm{bisq}^{x})(\mathrm{TFA})_3$ as well as the product Me−TFA and regenerated $\mathrm{OVCl_3}$. Either way, the final relative energy of the $\mathrm{Rh^{III}}(\mathrm{bisq}^{x})(\mathrm{TFA})_3$ complex is −13.7 kcal/mol at 298 K, which represents a completed cycle of the overall reaction $\mathrm{CH_4} + \mathrm{TFAH} \longrightarrow \mathrm{TFA{-}Me} + 2\,\mathrm{H^+} + 2\,\mathrm{e^-}$.

Finally, the I-III pathway was also investigated, starting from $\mathrm{Rh^{I}}(\mathrm{bisq}^{x})(\mathrm{TFA})(\mathrm{TFAH})$ as an

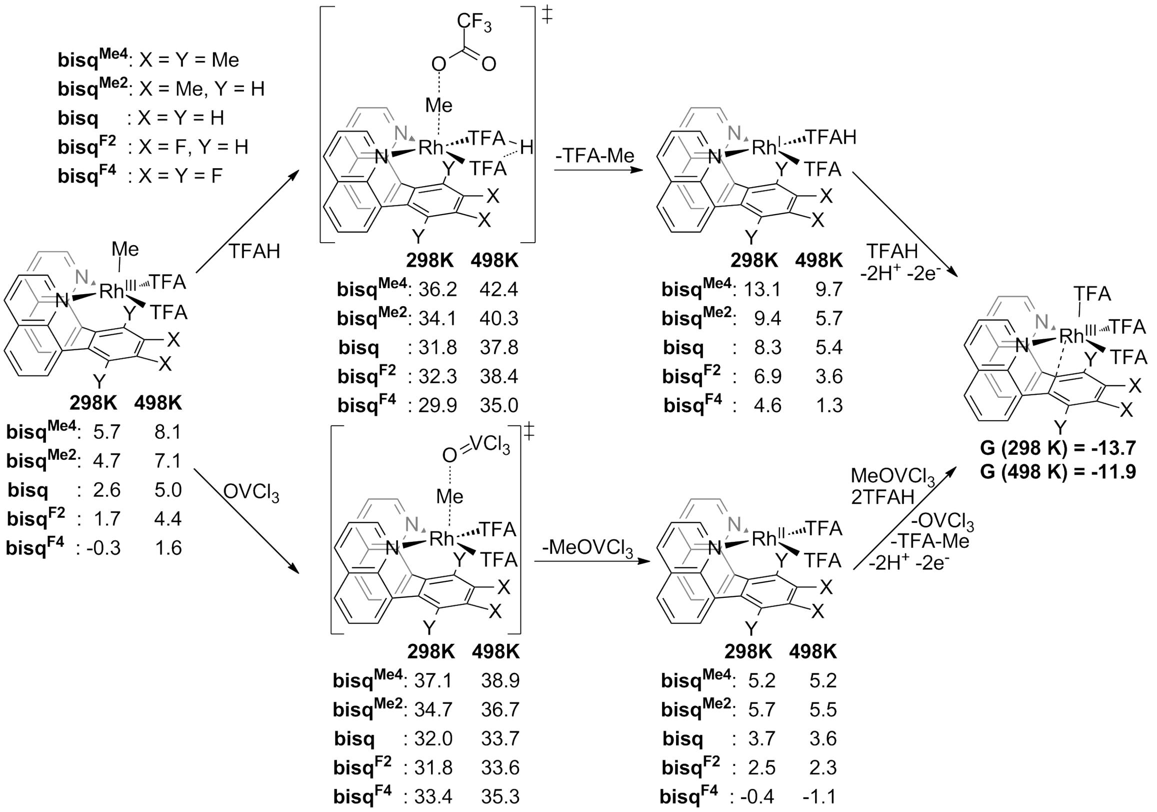

Scheme 3.19. Comparison of the functionalization of Rh^{III}(bisq^{x})(Me$_{ax}$)(TFA)$_2$, the lowest Rh−Me species, *via* the III-I S$_N$2 and III-II S$_R$2 pathways; and the completion of the catalytic cycle. Only the lowest functionalization transition state is shown for each pathway.

alternative ground state. The results are shown in Scheme 3.20. Although the oxidative addition of methane by $Rh^{I}(bisq^{x})$ species was feasible with minimum transition states of 27.9-30.6 depending on the particular ligand, the resulting $Rh^{I}(bisq^{x})(H)(Me)(TFA)$ species are very uphill in energy. Deprotonation to form a $Rh^{I}-Me$ species was prohibitively uphill both kinetically and thermodynamically. Along with the fact that $Rh^{I}(bisq^{x})$ species would be less stable than their $Rh^{III}(bisq^{x})$ analogues at reaction conditions, we did not pursue this route further.

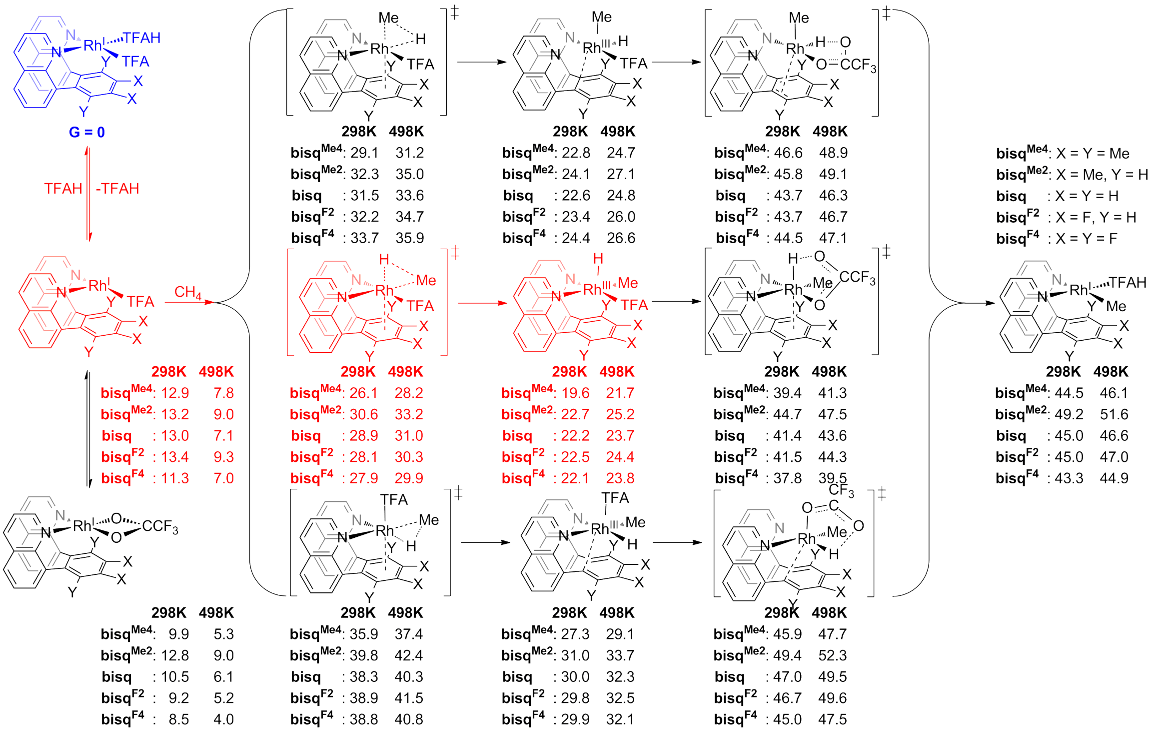

Scheme 3.20. Catalytic cycle for the activation and functionalization of methane using $Rh(bisq^{x})$ complexes in TFAH, *via* the Rh(I-III) pathway. Blue denotes the resting state and red the most favored pathway. All free energies are in kcal/mol.

By plotting the activation and transition state energies of the various $Rh^{III}(bisq^{x})$ ligands, we can determine the particular ligand with the optimal activity. The results are shown in Figure 3.7, and show convincingly that at both 298 K and 498 K, whether using the III-I or III-II pathway, the base ligand $Rh^{III}(bisq)$ is the best choice.

In comparing the relative merits of the III-I and III-II pathways, the energies of the two transition states at 298 K are very close, within 1 kcal/mol for each $(bisq^{x})$ ligand (although, as mentioned before, $(bisq^{F4})$ appears to be an outlier). However, the energies are expected to increase at 498 K, due to the increased entropy penalty of bringing an extra TFAH or $OVCl_3$ to the system. For the III-I S_N2 pathway, this is a significant penalty of 6.0-6.2 kcal/mol, and may be enough to render functionalization inaccessible. However, for the III-II S_R2 pathway the entropy penalty is much less at 1.7-2.0 kcal/mol, and both the base (bisq) and fluorinated $(bisq^{F2})$ and $(bisq^{F4})$ have barriers at

Figure 3.7. *Top*: graph of the activation and III-I functionalization transition state energies of the various Rh(bisq^x) complexes. The best choice at both 298 K and 498 K is the base Rh(bisq) complex. This complex has a maximum barrier of 33.4 kcal/mol at 298 K and 37.8 kcal/mol at 498 K. The rate-determining step is activation at 298 K and functionalization at 498 K. *Bottom*: graph of the activation and III-II functionalization transition state energies of the various Rh(bisq^x) complexes. Again, the best choice at both 298 K and 498 K is the base Rh(bisq) complex. This complex has a maximum barrier of 33.4 kcal/mol at 298 K and 35.8 kcal/mol at 498 K. The rate-determining step is methane activation at both temperature points. *Both*: Blue diamond markers and lines denote transition state energies at 298 K, and red square markers and lines at 498 K. Outline marker shapes denote activation transition states and filled marker shapes denote functionalization transition states. The overall barrier for each particular complex is the greater of the activation and functionalization barriers.

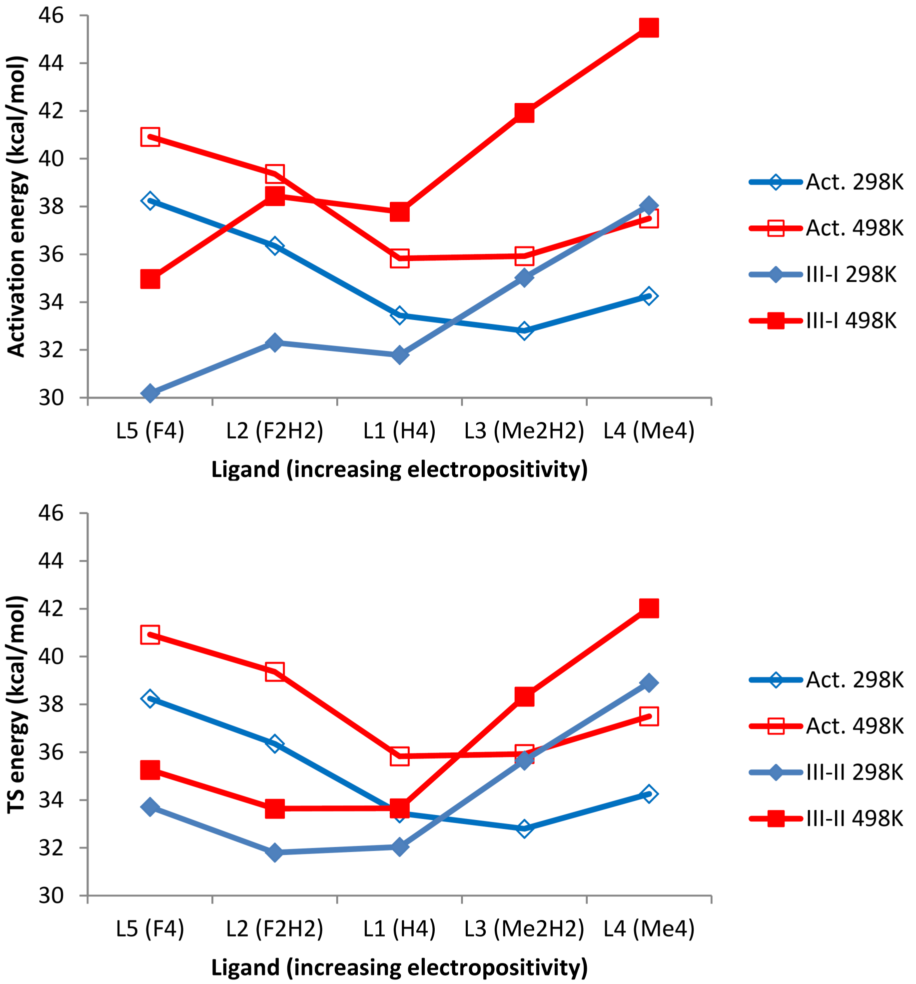

35.3 kcal/mol or below. Thus it appears that the III-II S_R2 pathway is the best choice for methyl functionalization.

Hence, we conclude that the base Rh(bisq) rhodium-ligand complex is the best choice among the entire Rh(bisq^x) family, with an overall reaction barrier of 33.4 kcal/mol at 298 K and 35.8 kcal/mol at 498 K, when the III-II S_R2 functionalization pathway is used.

3.4.8 Product protection and C−H activation

As mentioned in the introduction, a major hurdle that any putative methane to methanol catalytic scheme must overcome arises because the C−H bond dissociation energy of methanol is 9 kcal/mol weaker than that of methane. Preventing the overoxidation of the product is thus a challenge and is the reason we elected to investigate electrophilic metal centers in acidic solvent. Since the transition state of an electrophilic activation involves donation of electron density from the methane C−H σ bond to the metal, a highly electron-withdrawing trifluoroacetate substituent that decreases this σ bond electron density is expected to increase the transition state energy. Thus the highly electronegative trifluoroacetate group of methyl trifluoroacetate withdraws electron density from the methyl C−H bonds, thereby decreasing their ability to donate into the rhodium center and raising activation barriers.

Indeed, we see this effect in explicit calculations with both the (NN) and (NN^F) ligand sets. Figures 3.8 and 3.9 show the various isomeric transition states for the activation of both methane and methyl trifluoroacetate in TFAH. At 298 K, each transition state for the activation of methane was 3 to 10 kcal/mol lower than the corresponding transition state for the activation of methyl trifluoroacetate (1 atm reference for both). The first two rows of Figure 3.10 show only the lowest energy isomer of each activation, and thus an overall $\Delta G^\ddagger$ (lowest Me−TFA transition state minus lowest CH_4 transition state) of 2.7 kcal/mol is found for (NN) and 5.5 kcal/mol for (NN^F). The numbers significantly improve to 6.4 and 9.8 kcal/mol at 498 K. This is due to the volatility of Me−TFA, which greatly raises its free energy at 498 K.

In contrast, activation of methanol (1 M reference state) by Rh(NN^F), shown in Figure 3.11 and summarized in the third row of Figure 3.10, was even lower than that of methane: by 0.3 or 1.8 kcal/mol at 298 K when comparing the lowest CH_3OH transition state and the lowest CH_4 transition state in TFAH (Figure 3.10, first and second rows); for (NN^F) in water this gap is larger at 2 to 3 kcal/mol (Figure 3.10, third row). We can explain this by noting that the hydroxyl group in methanol has electron donating properties and hence the donation effect of the C−H σ orbital into the electrophilic metal center is increased, leading to a decreased transition state barrier; however these numbers are lower than the 9 kcal/mol simple BDE difference between the C−H bonds in methane and methanol and comparable to work done by Owen et al. [23].

Product protection studies were also carried out for the Rh(DPMS) and Rh(DPES) complexes,

Figure 3.8. Transition states for the functionalization of methane, Me−TFA, and methanol using Rh(NN) complexes in TFAH. All free energies are in kcal/mol and relative to the lowest energy inorganic state (i.e. right before methane activation).

(NN) ligand

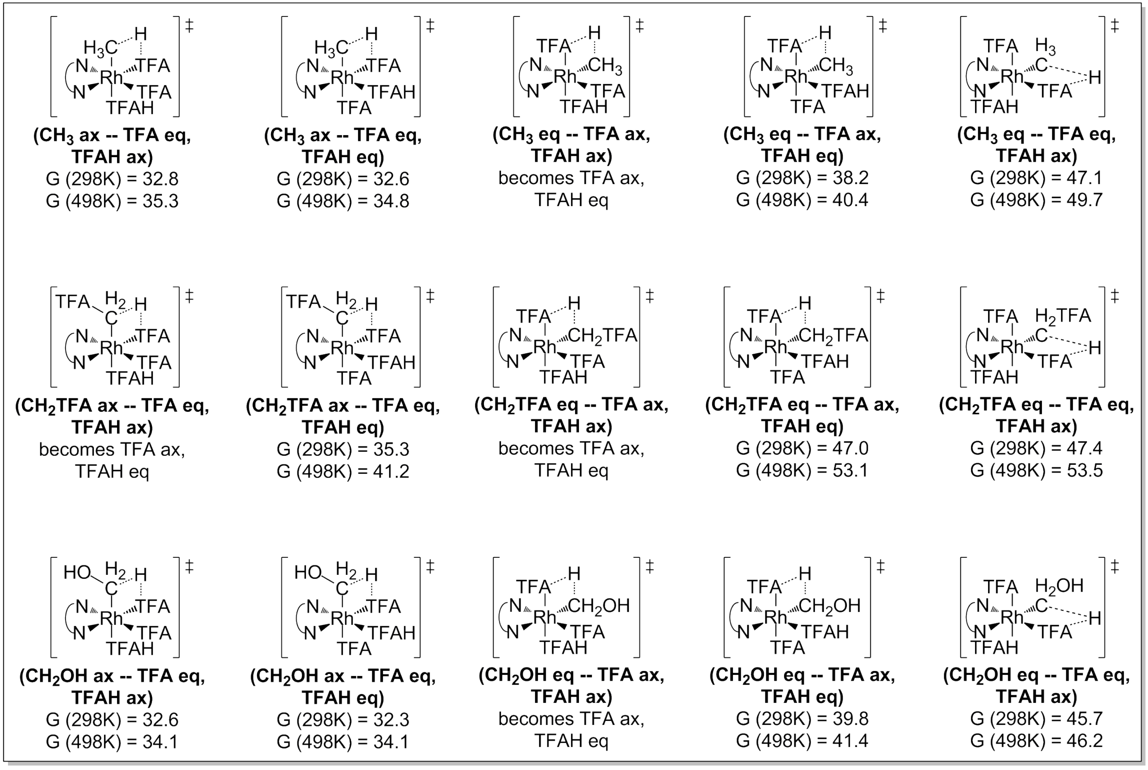

(CH_3 ax -- TFA eq, TFAH ax)
G (298K) = 32.8
G (498K) = 35.3

(CH_3 ax -- TFA eq, TFAH eq)
G (298K) = 32.6
G (498K) = 34.8

(CH_3 eq -- TFA ax, TFAH ax)
becomes TFA ax, TFAH eq

(CH_3 eq -- TFA ax, TFAH eq)
G (298K) = 38.2
G (498K) = 40.4

(CH_3 eq -- TFA eq, TFAH ax)
G (298K) = 47.1
G (498K) = 49.7

(CH_2TFA ax -- TFA eq, TFAH ax)
becomes TFA ax, TFAH eq

(CH_2TFA ax -- TFA eq, TFAH eq)
G (298K) = 35.3
G (498K) = 41.2

(CH_2TFA eq -- TFA ax, TFAH ax)
becomes TFA ax, TFAH eq

(CH_2TFA eq -- TFA ax, TFAH eq)
G (298K) = 47.0
G (498K) = 53.1

(CH_2TFA eq -- TFA eq, TFAH ax)
G (298K) = 47.4
G (498K) = 53.5

(CH_2OH ax -- TFA eq, TFAH ax)
G (298K) = 32.6
G (498K) = 34.1

(CH_2OH ax -- TFA eq, TFAH eq)
G (298K) = 32.3
G (498K) = 34.1

(CH_2OH eq -- TFA ax, TFAH ax)
becomes TFA ax, TFAH eq

(CH_2OH eq -- TFA ax, TFAH eq)
G (298K) = 39.8
G (498K) = 41.4

(CH_2OH eq -- TFA eq, TFAH ax)
G (298K) = 45.7
G (498K) = 46.2

Figure 3.9. Transition states for the functionalization of methane, Me−TFA, and methanol using Rh(NN^F) complexes in TFAH. All free energies are in kcal/mol and relative to the lowest energy inorganic state (i.e. right before methane activation).

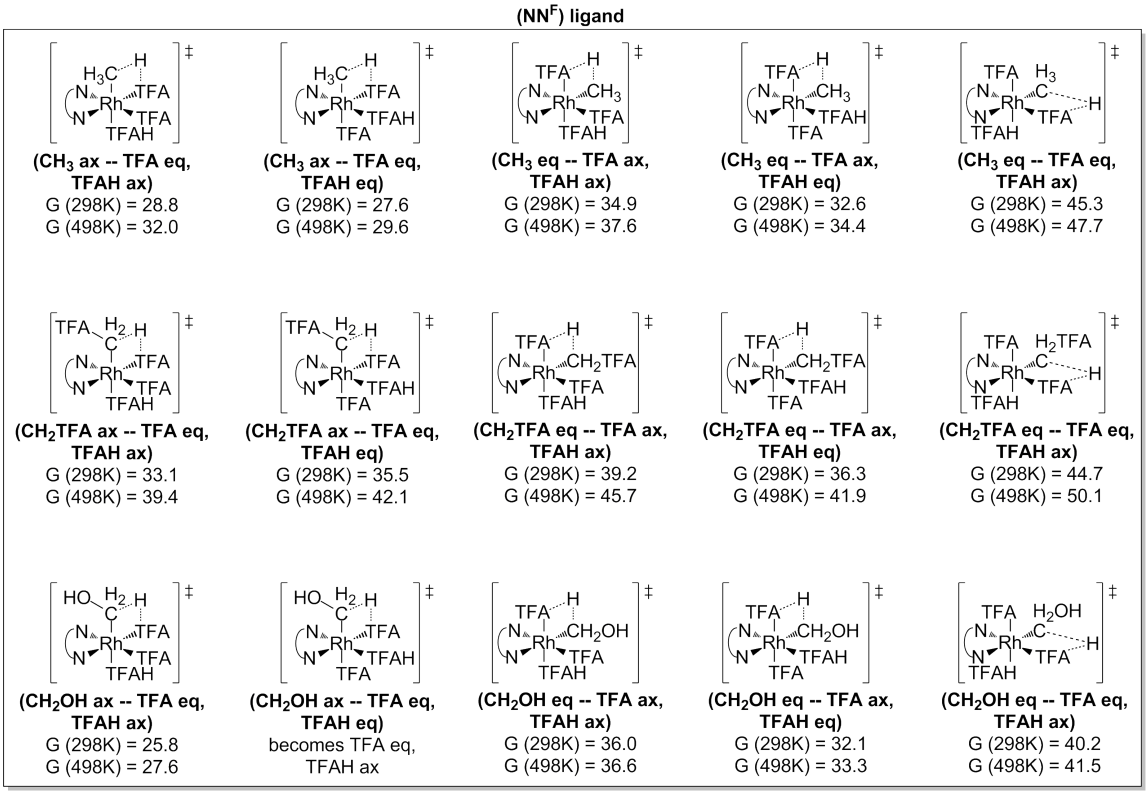

Figure 3.10. Summary of the data presented in Figures 3.8, 3.9, and 3.11. In each row, the leftmost structure is the lowest-energy activation transition state for methane (1 atm); the center structure is the lowest-energy transition state for the activation of MeTFA (1 atm, not applicable for the H_2O case); and the rightmost structure is the lowest-energy transition state for the activation of MeOH (1 atm). All free energies are in kcal/mol and relative to the lowest energy inorganic state (i.e. right before methane activation).

(NN) ligand in TFAH

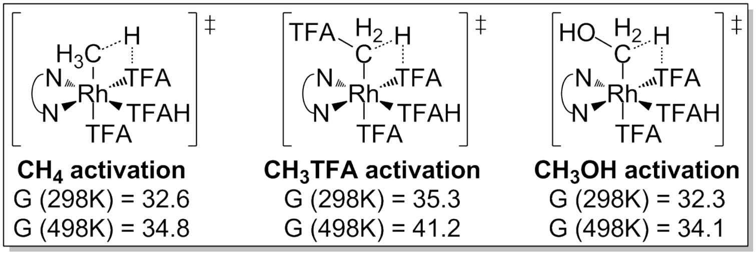

(NN^F) ligand in TFAH

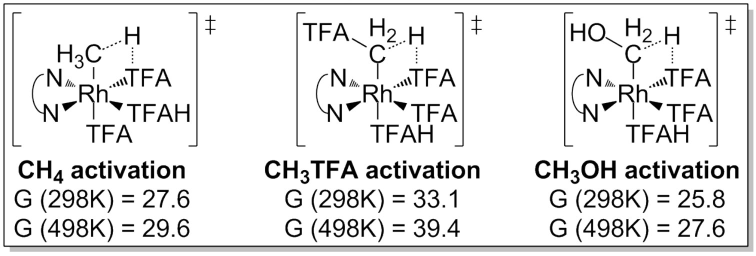

(NN^F) ligand in H_2O

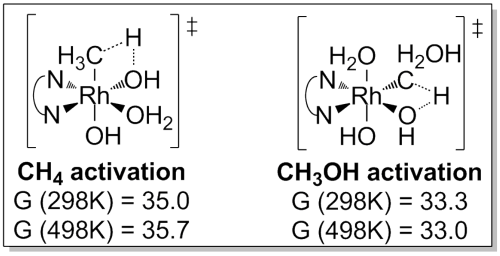

Figure 3.11. Comparison of activation energies for methane (1 atm) and for methanol (1 M at 298 K, 1 atm at 498 K) in the same structure for Rh(NN^F) complexes in water. In this case, methanol was easier to activate by 2 to 3 kcal/mol. All free energies are in kcal/mol and relative to the lowest energy inorganic state (i.e. right before methane activation).

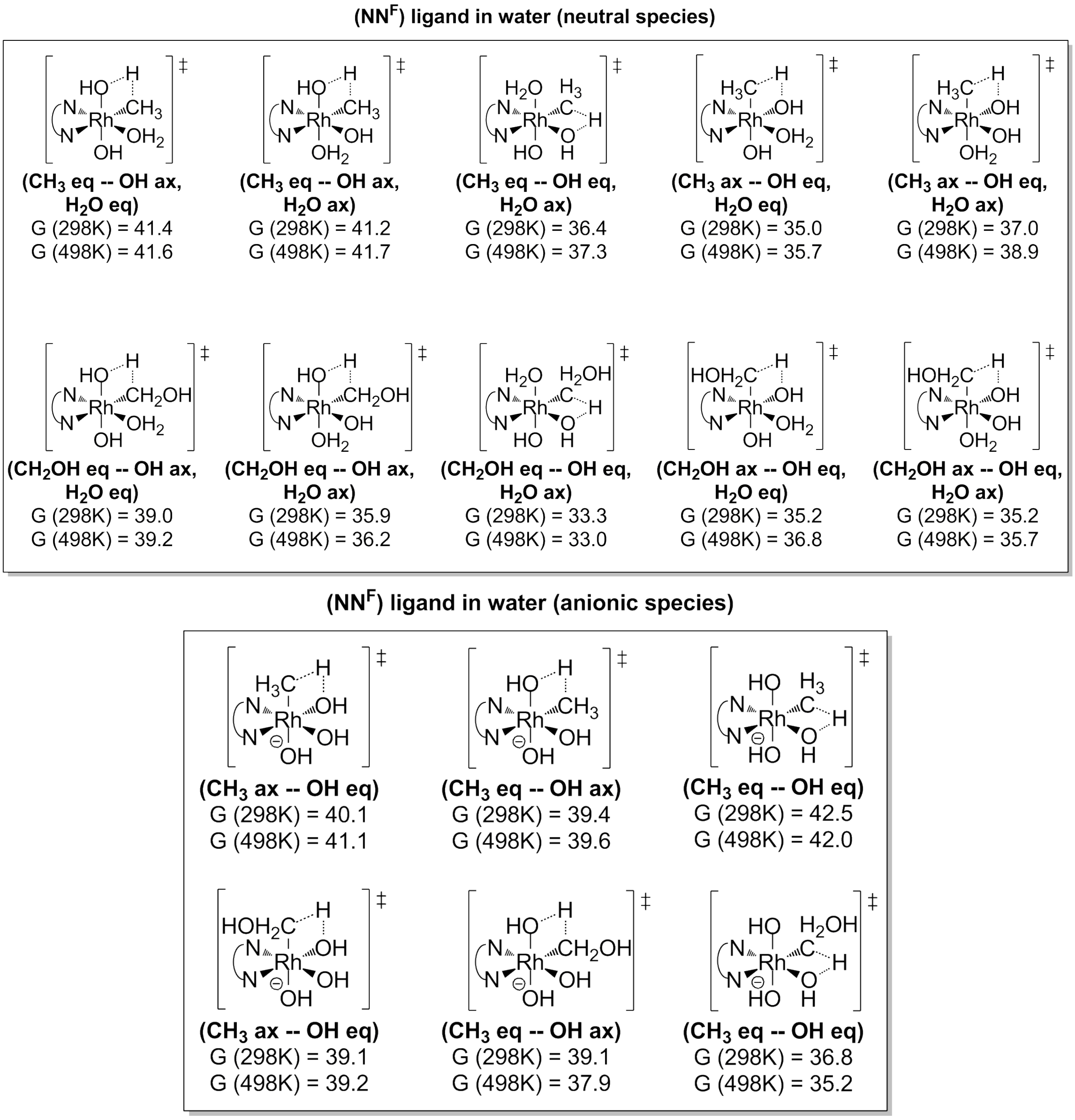

the results of which are shown in Figures 3.12 and 3.13, respectively. Modest product protection $\Delta\Delta G^{\ddagger}$'s of 1.4 kcal/mol and 2.2 kcal/mol at 298 K were found, but these improve to 5.3 kcal/mol and 6.6 kcal/mol at 498 K.

Figure 3.12. Comparison of the activation states of methane and methyl trifluoroacetate by Rh(DPMS) complexes, showing the product protection afforded. Red denotes the most favored isomer of each type of activation. All free energies are in kcal/mol and relative to the resting state.

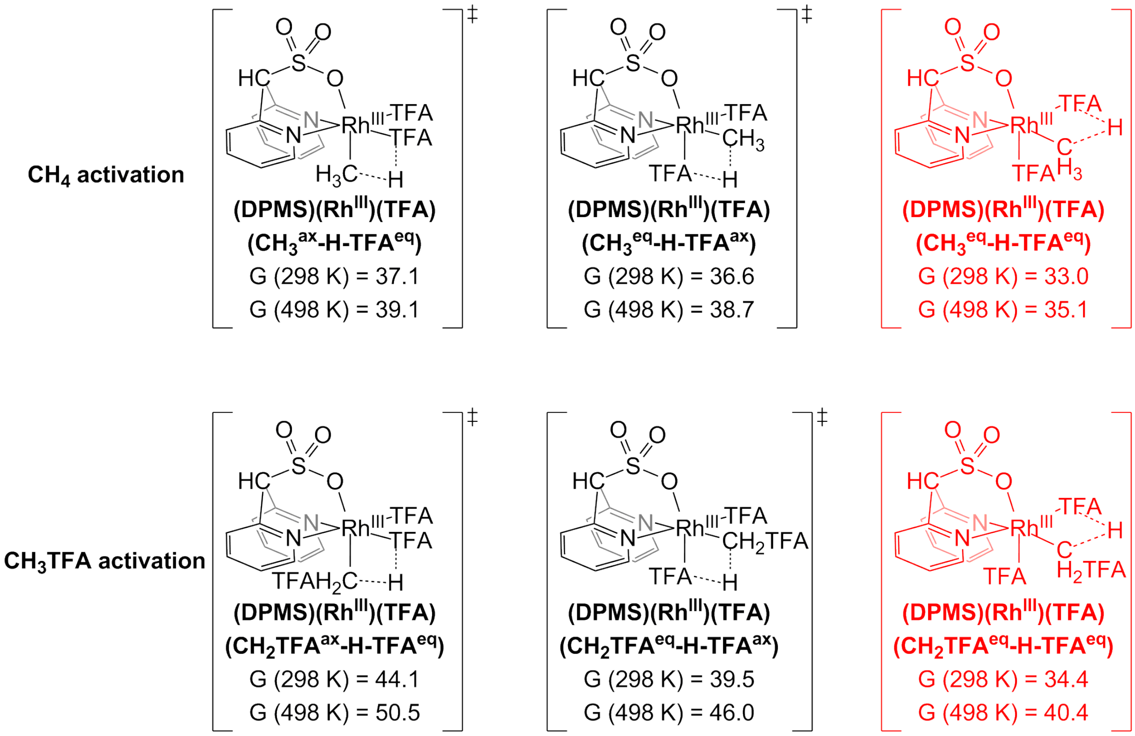

Finally, product protection studies were carried out for the Rh(bisq^{x}) family of rhodium-ligand complexes. The results are summarized in Figure 3.14. In general the product protection is comparable to the Rh(NN^{x}) family at 298 K, but improves significantly by 3.8-4.2 kcal/mol at 498 K. As in the other cases, this is due to the high volatility of Me−TFA.

Since the ease of activation decreases $CH_3OH > CH_4 >$ Me−TFA, it is important to consider the relative chemical potential of CH_3OH and Me−TFA in solution. As we have found that the equilibrium $\mathrm{Me{-}TFA}(g) + H_2O(solv) \rightleftharpoons CH_3OH(g) + \mathrm{TFAH}(\ell)$ is exergonic by 1.3 kcal/mol at 298 K, it is predicted that these catalysts would be selective for methane oxidation only in the absence of water.

In comparison with previous work, we note that Periana et al. [24] showed that the reason why the Catalytica-Periana bipyrimidine Pt catalyst [25] was able to achieve high selectivity is that the barrier to activate the Me−OSO_3H product is 14 kcal/mol higher than for CH_4 or CH_3OH and the acidity of the medium drives the protection of methyl products *via* esterification. Although

Figure 3.13. Comparison of the activation states of methane and methyl trifluoroacetate by Rh(DPES) complexes, showing the product protection afforded. Red denotes the most favored isomer of each type of activation. All free energies are in kcal/mol and relative to the resting state.

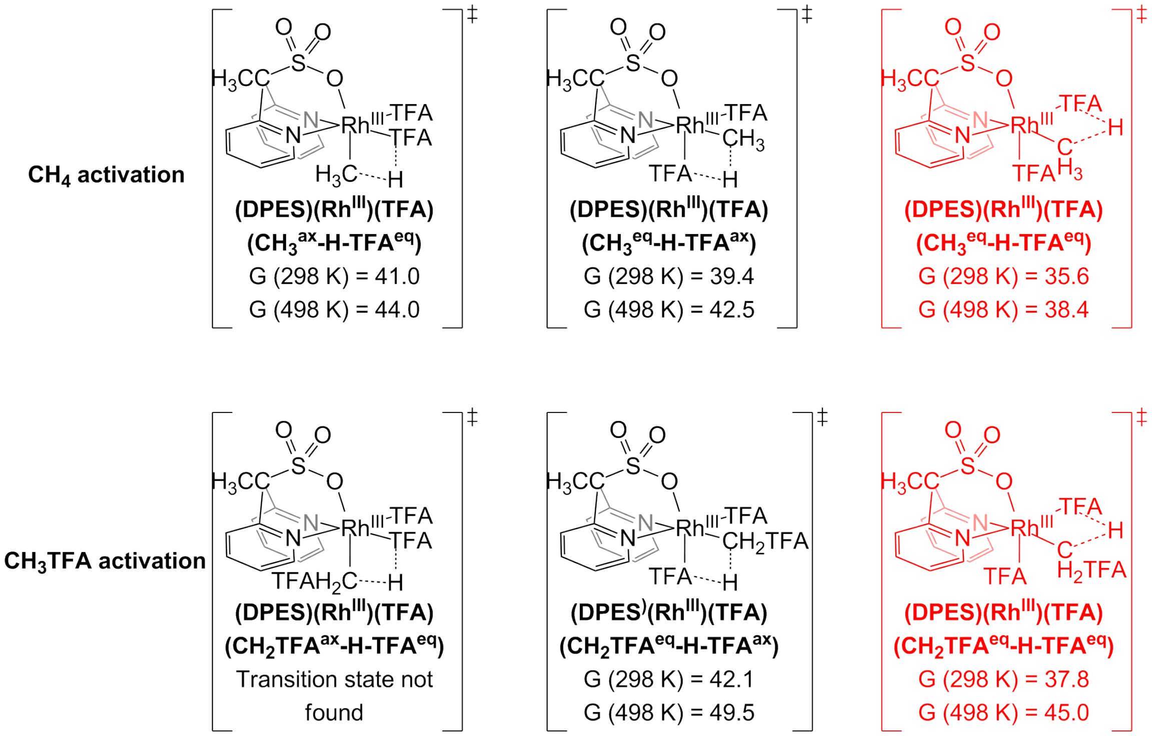

Figure 3.14. Comparison of the activation states of methane and methyl trifluoroacetate by the Rh(bisq^x) family of complexes, showing the product protection afforded. Red denotes the most favored isomer of each type of activation. The overall product protection $\Delta\Delta G^\ddagger$ energies are shown in blue. All free energies are in kcal/mol and relative to the resting state.

bisq$^{\mathrm{Me4}}$: X = Y = Me
bisq$^{\mathrm{Me2}}$: X = Me, Y = H
bisq : X = Y = H
bisq$^{\mathrm{F2}}$: X = F, Y = H
bisq$^{\mathrm{F4}}$: X = Y = F

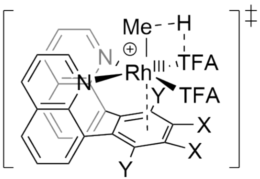

	298K	**498K**
bisq$^{\mathrm{Me4}}$	38.9	41.3
bisq$^{\mathrm{Me2}}$	37.8	40.3
bisq	38.3	40.7
bisq$^{\mathrm{F2}}$	39.3	42.4
bisq$^{\mathrm{F4}}$	40.4	43.0

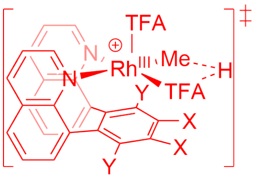

	298K	**498K**
bisq$^{\mathrm{Me4}}$	32.4	34.4
bisq$^{\mathrm{Me2}}$	31.8	34.3
bisq	33.4	35.8
bisq$^{\mathrm{F2}}$	36.4	39.4
bisq$^{\mathrm{F4}}$	38.2	40.9

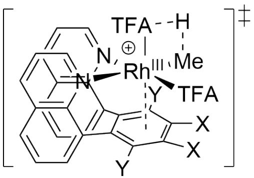

	298K	**498K**
bisq$^{\mathrm{Me4}}$	39.1	41.3
bisq$^{\mathrm{Me2}}$	37.7	40.3
bisq	39.1	41.9
bisq$^{\mathrm{F2}}$	40.5	43.3
bisq$^{\mathrm{F4}}$	43.2	45.7

PRODUCT PROTECTION

	298K	**498K**
bisq$^{\mathrm{Me4}}$	6.7	11.3
bisq$^{\mathrm{Me2}}$	4.5	8.3
bisq	3.9	8.1
bisq$^{\mathrm{F2}}$	3.1	6.9
bisq$^{\mathrm{F4}}$	6.2	10.2

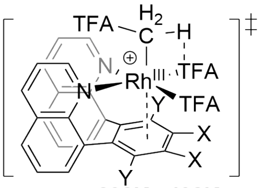

	298K	**498K**
bisq$^{\mathrm{Me4}}$	41.9	48.1
bisq$^{\mathrm{Me2}}$	42.3	48.7
bisq	41.9	48.2
bisq$^{\mathrm{F2}}$	44.7	51.2
bisq$^{\mathrm{F4}}$	47.3	53.9

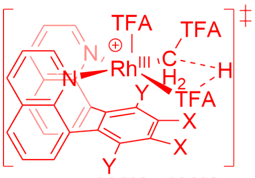

	298K	**498K**
bisq$^{\mathrm{Me4}}$	39.1	45.7
bisq$^{\mathrm{Me2}}$	36.3	42.6
bisq	37.3	43.9
bisq$^{\mathrm{F2}}$	39.5	46.3
bisq$^{\mathrm{F4}}$	44.4	51.1

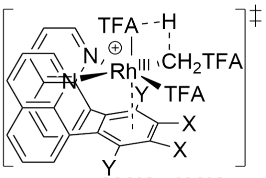

	298K	**498K**
bisq$^{\mathrm{Me4}}$	39.4	45.8
bisq$^{\mathrm{Me2}}$	39.9	46.7
bisq	38.5	45.2
bisq$^{\mathrm{F2}}$	42.0	48.7
bisq$^{\mathrm{F4}}$	46.5	52.7

the Catalytica-Periana system distinguishes between methane and the methyl ester more than the rhodium complexes, we note that a key advantage to our system is the volatility of CH_3OH and Me−TFA (boiling points at 64.7°C and 43°C, respectively) relative to the nonvolatile Me−OSO_3H. Increasing selectivity beyond what is provided by the electrophilicity of the metal and esterification is still an important area of research. The addition of nonpolar ligand side-chains may decrease the propensity of methanol coordination to the metal relative to methane coordination.

3.5 Discussion

Since our ligands have poor electron-donating ability and Rh^{III}-centered cycles, we expect the metal center to be electrophilic with reactions proceeding along an electrophilic route [3]h. We can rule out oxidative addition due to the nature of our ligands and the general instability of Rh^{V} species; hence we expected that the most likely C−H activation pathway is through a base-mediated electrophilic mechanism (Scheme 3.21).

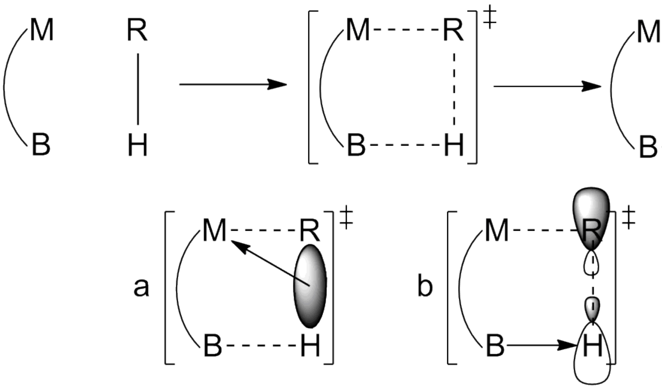

Scheme 3.21. A schematic diagram showing the metal activation of an R−H bond, for example, methane. Activation occurs *via* ligand donation to the electrophilic metal center (a) and basic abstraction of the hydrogen (b).

Because we propose an electrophilic pathway for the methane activation step [3]h, we expect there to be a relationship between the activation transition state energy and some aspect of the metal's electropositivity. To find this relationship, we examined more deeply the calculated constituent energies of rhodium complexes with the (NN^{x}), (ONN^{x}), ($DP\frac{M}{E}S$), and (PN) ligands and ligand families. We did not include the L_3 ($bisq^{x}$) family because they require protonation before methane activation can take place; as a result a direct comparison of these ligands with the neutral transition states of our other ligands is not possible.

To estimate the electropositivity, we initially used the calculated energy of the rhodium 4*s* core orbital in the Rh^{III} resting state, which we compared to the corresponding methane activation energies (Figure 3.15). We found that there is approximately a positive correlation between increasing electropositivity (as measured by negative numbers closer to zero) and increase overall transition state barriers. We explain this by noting that decreasing the metal's electropositivity increases its electrophilicity and thus encourages σ donation of the Me−H bond.

Figure 3.15. Graph of the methane activation energy of the various rhodium complexes *vs.* the 4*s* orbital energy of the rhodium in their resting states, based on data from Table 3.3. This calculated value is a proxy for the relative overall electropositivity of the specific rhodium-ligand complexes. In all cases the lowest transition state was used; this involves an axial Rh−Me being formed in the cases of the (NN^x) and (ONN^x) ligand families, and an equatorial Rh−Me being formed in the ($DP\frac{M}{E}S$) and (PN) cases.

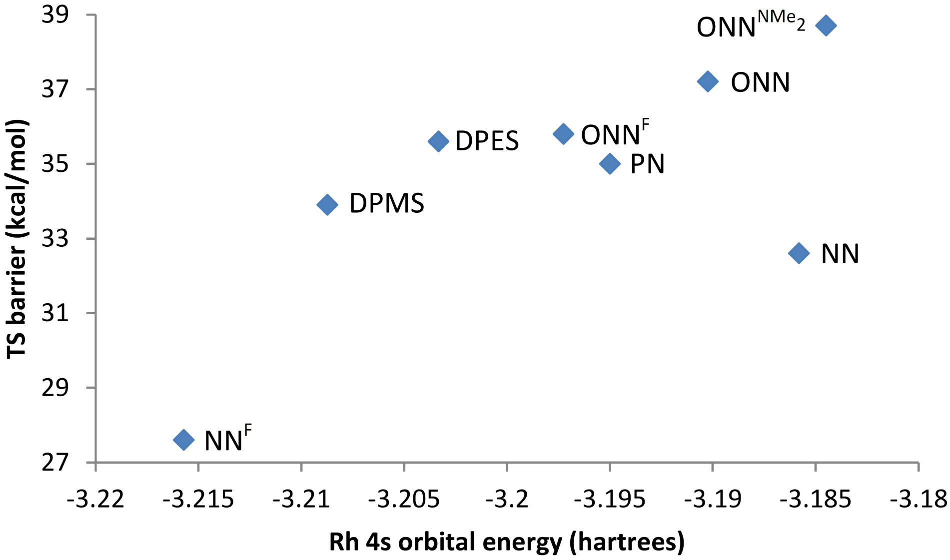

In the hopes that a more directional aspect of a given rhodium-ligand's electron density might give us a better correlation with the transition state barrier, we then plotted the methane activation energies with the energies of the Rh−C bond in the resultant Rh^{III}−Me intermediate (Figure 3.16). These Rh−C bond energies were obtained by performing a Pipek-Mezey orbital localization procedure on the Rh^{III}−Me complex's electronic wavefunction [13]. We found that the correlation is much better, with increasingly negative Rh−C bond energies being correlated with decreasing transition state barriers. This may be due to the increasing favorability of forming the rhodium-methyl bond. We give the caveat that again the only outlier is the Rh(NN) ligand complex, but we note that our trend represents only an overestimation, and therefore does not include false positives. In addition, there is a definite positive correlation within a ligand family (i.e. Rh(NN) *vs.* Rh(NN^F); Rh(ONN^F) *vs.* Rh(ONN) *vs.* Rh(ONN^{NMe_2})). We conclude from this relationship that (a) given a rhodium-ligand complex that already shows some promise, we can further fine-tune its properties with additional modifications on the ligand to further lower the transition state barriers of interest; and (b) given a new rhodium-ligand complex, by calculating the Rh^{III}−Me intermediates and extracting the Rh−C bond energy, we can get an estimate of the expected methane activation transition state barrier for that ligand set and thus gauge its worthiness for further investigation.

Ligand	TS^a	$\Delta G^b_{\text{precursor}}$	Precursor^c
(NN)	32.6	1.3	$[\text{Rh}^{\text{III}}(\text{NN})(\text{TFA})_4]^{2-}(\text{H}^+_{\text{ax}})(\text{H}^+_{\text{eq}})$
(NN$^{\text{F}}$)	27.6	2.2	$[\text{Rh}^{\text{III}}(\text{NN}^{\text{F}})(\text{TFA})_4]^{2-}(\text{H}^+_{\text{ax}})(\text{H}^+_{\text{eq}})^j$
(ONN)	37.2	3.9	$[\text{Rh}^{\text{III}}(\text{ONN})(\text{TFA})_3]^{-}(\text{H}^+_{\text{ax}})$
(ONN$^{\text{F}}$)	35.8	4.0^k	$[\text{Rh}^{\text{III}}(\text{ONN}^{\text{F}})(\text{TFA})_3]^{-}(\text{H}^+_{\text{ax}})^l$
(ONN$^{\text{NMe}_2}$)	38.7	3.7	$[\text{Rh}^{\text{III}}(\text{ONN}^{\text{NMe}_2})(\text{TFA})_3]^{-}(\text{H}^+_{\text{ax}})$
(DPMS)	33.9	0.0	$[\text{Rh}^{\text{III}}(\text{DPMS})(\text{TFA})_3]^{-}(\text{H}^+_{\text{eq}})$
(DPES)	35.6	0.0	$[\text{Rh}^{\text{III}}(\text{DPES})(\text{TFA})_3]^{-}(\text{H}^+_{\text{eq}})$
(PN)	35.0	N/A^m	$[\text{Rh}^{\text{III}}(\text{PN})(\text{TFA})_3]^{-}(\text{H}^+_{\text{N}})^l$

Ligand	Adj. TS^d	Rh−C σ^e	Rh−Me^f	Rh−TFA 4s^g	Rh−Me 4s^h	$\Delta 4s^i$
(NN)	31.3	−0.38096	$[\text{Rh}^{\text{III}}(\text{NN})(\text{Me}_{\text{ax}})(\text{TFA})_3]^{2-}(\text{H}^+_{\text{ax}})(\text{H}^+_{\text{eq}})$	−3.1858	−3.13265	0.05315
(NN$^{\text{F}}$)	25.4	−0.39557	$[\text{Rh}^{\text{III}}(\text{NN}^{\text{F}})(\text{Me}_{\text{ax}})(\text{TFA})_3]^{2-}(\text{H}^+_{\text{ax}})(\text{H}^+_{\text{eq}})^j$	−3.21571	−3.15195	0.06376
(ONN)	33.3	−0.37870	$[\text{Rh}^{\text{III}}(\text{ONN})(\text{Me}_{\text{ax}})(\text{TFA})_2]^{-}(\text{H}^+_{\text{ax}})$	−3.19023	−3.13949	0.05074
(ONN$^{\text{F}}$)	31.8	−0.38498	$[\text{Rh}^{\text{III}}(\text{ONN}^{\text{F}})(\text{Me}_{\text{ax}})(\text{TFA})_2]^{-}(\text{H}^+_{\text{ax}})$	−3.19724	−3.14661	0.05063
(ONN$^{\text{NMe}_2}$)	35.0	−0.37739	$[\text{Rh}^{\text{III}}(\text{ONN}^{\text{NMe}_2})(\text{Me}_{\text{ax}})(\text{TFA})_2]^{-}(\text{H}^+_{\text{ax}})$	−3.18448	−3.13750	0.04698
(DPMS)	33.9	−0.38700	$[\text{Rh}^{\text{III}}(\text{DPMS})(\text{Me}_{\text{eq}})(\text{TFA})_2]^{-}(\text{H}^+_{\text{eq}})$	−3.20873	−3.15703	0.05170
(DPES)	35.6	−0.38539	$[\text{Rh}^{\text{III}}(\text{DPES})(\text{Me}_{\text{eq}})(\text{TFA})_2]^{-}(\text{H}^+_{\text{eq}})$	−3.20332	−3.15567	0.04765
(PN)	N/A^m	−0.38515	$[\text{Rh}^{\text{III}}(\text{PN})(\text{Me}_{\text{N}})(\text{TFA})_3]^{-}(\text{H}_{\text{P}})$	−3.19499	−3.15474	N/A^m

Table 3.3. Comparison of the various Rh parameters with the rhodium-ligands complexes' associated transition state barriers. These numbers are plotted in Figures 3.15, 3.16, and 3.17. An "ax" subscript indicates that the moiety is axial with respect to the rhodium-ligand plane; An "eq" subscript indicates that the moiety is equatorial with respect to the rhodium-ligand plane. For (DP$\frac{\text{M}}{\text{E}}$S) the rhodium-ligand plane is defined as the plane spanned by the N−Rh−N moiety. For (PN) complexes, An "N" subscript indicates that the moiety is equatorial with respect to the P−Rh−N plane and *trans* to the N; A "P" subscript indicates that the moiety is equatorial with respect to the P−Rh−N plane and *trans* to the P. (a) The overall transition state barrier, as reproduced from Table 3.2, in kcal/mol. (b) The free energy of the immediate precursor before the lowest methane activation barrier, in kcal/mol. This typically differs from the resting state only in the geometric placement of TFAH and TFA ligands. (c) The identity of the immediate precursor. (d) The "adjusted" TS barrier, i.e. the free energy change of the actual transition state itself, in kcal/mol. Equal to the overall TS − $G_{\text{precursor}}$. (e) The energy of the Pipek-Mezey localized Rh−C bond of the Rh$^{\text{III}}$−Me species formed as a result of the lowest transition state, in hartrees. (f) The identity of the Rh$^{\text{III}}$−Me species formed as a result of the lowest transition state. (g) The 4s orbital energy of the Rh atom in the resting state, in hartrees. (h) The 4s orbital energy of the Rh atom in the Rh$^{\text{III}}$−Me species in column f, in hartrees. (i) The change in Rh 4s energies, equal to the difference between the preceding two columns, in hartrees. (j) These species are the lowest neutral species, done for the sake of consistency with the other ligands. The anionic resting states are very similar in energy. (k) An estimated value based on the $G_{\text{precursor}}$ values of related species Rh(ONN) and Rh(ONN$^{\text{NMe}_2}$). (l) Stable conformations of these complexes could not be found due to the ease of isomerization of the TFAH/TFA ligands into axial/equatorial positions. (m) The value is unknown and an estimation was not attempted.

Figure 3.16. Graph of the methane activation energy of the various rhodium complexes *vs.* the Rh−C bond energy as localized by the Pipek-Mezey method [13] of the lowest-energy Rh−Me complex. This calculated value is a proxy for the relative directional electropositivity of the specific rhodium-ligand complexes towards the methyl bond being formed. Based on data from Table 3.3. In all cases the lowest transition state was used; this involves an axial Rh−Me being formed in the cases of the (NN^x) and (ONN^x) ligand families, and an equatorial Rh−Me being formed in the $(\mathrm{DP}\frac{\mathrm{M}}{\mathrm{E}}\mathrm{S})$ and (PN) cases.

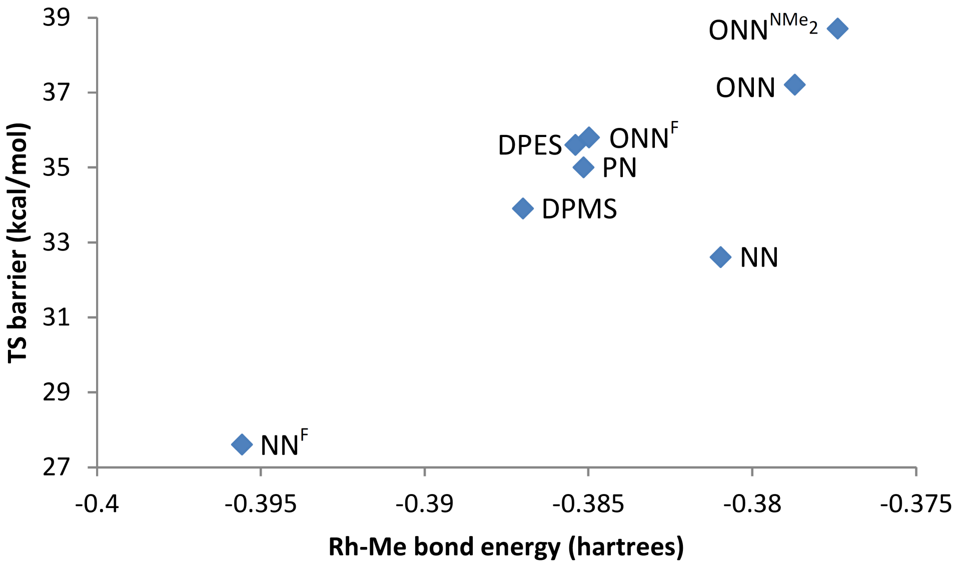

We also wished to see if there was a correlation between the transition state barrier and the rhodium center's hardness as modified by its ligand. Since the hardness of an atom or molecule is defined as the polarizability of its electron cloud [26], we measured the difference in the Rh 4*s* orbital energy going from the inorganic resting state to the $\mathrm{Rh}^{\mathrm{III}}$−Me as a proxy for hardness. Although we did not find a correlation with the overall transition state barrier of activation, we did find a negative correlation with the "adjusted" TS barrier, i.e. the free energy change of the actual transition state itself (Figure 3.17). In other words, the activation transition state $[\mathrm{Rh}\cdots\mathrm{CH}_4]^{\ddagger}$ is derived from the replacement of a TFAH ligand with CH_4, but the immediate Rh−TFAH precursor is not the resting state, but differs slightly in its axial/equatorial arrangement of TFAH/TFA ligands and is a few kcal/mol higher in energy. Taking this out gives us our correlation. Hence, we see that increased polarizability or softness, as measured by the amount of energy increase in the rhodium-ligand system when a TFA ligand is exchanged for a methyl, correlates with a lower activation barrier.

The result of our fine tuning has yielded, among those rhodium-ligand complexes with neutral activation transition states, the $(\mathrm{NN}^{\mathrm{F}})$ ligand set. With a methane activation energy of 27.6 kcal/mol at 298 K, it compares favorably with other homogeneous systems. Indeed, an effective activation barrier of 33.5 kcal/mol is derived from the turnover frequency of the Catalytica-Periana catalyst $(\mathrm{bpym})\mathrm{PtCl}_2$ in H_2SO_4 [27]. Specifically, C−H activation by $(\eta^3$-6-phenyl-2,2′-bipyridine$)\mathrm{Ir}^{\mathrm{III}}(\mathrm{TFA})$-$(\mathrm{C}_2\mathrm{H}_4)(\mathrm{C}_2\mathrm{H}_5)$ is shown to catalyze H/D exchange between CH_4 and TFAD with a turnover frequency

Figure 3.17. A graph of the Rh−TFA to Rh−Me change in the 4*s* orbital energy, a measure of the Rh atom's softness, versus the adjusted TS barrier (see text). Note that the (ONN^F) data point is an estimated value, which may explain its deviation from the monotonicity (see Table 3.3). In all cases the lowest transition state was used; this involves an axial Rh−Me being formed in the cases of the (NN^x) and (ONN^x) ligand families, and an equatorial Rh−Me being formed in the ($DP\frac{M}{E}S$) and (PN) cases. This graph is based on data from Table 3.3.

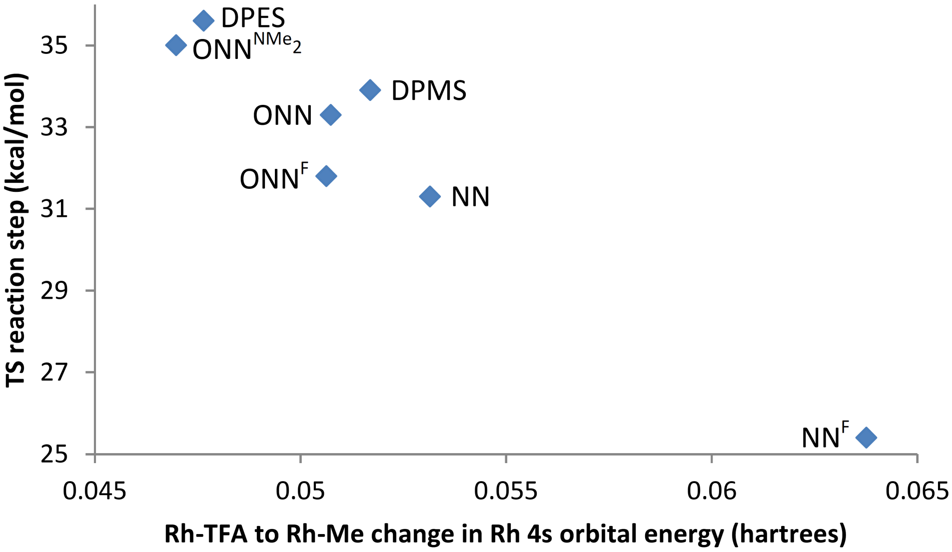

of 2.12×10^{-2} s^{-1} at 180°C (Scheme 3.18). From the turnover frequency a free energy barrier of 33.5 kcal/mol can be calculated using transition state theory [28].

In the course of these studies we found that it was more difficult to find effective routes of Rh-methyl functionalization than to find low methane activation barriers. We found that the III-II pathway (S_R2 attack with $OVCl_3$) typically gives the lowest barriers, whereas the III-I and III-IV-II pathway (S_N2 attack on Rh^{III} or Rh^{IV}, respectively) have some use as well; the I-III pathway (oxidative addition of methane by Rh^I) was much less likely.

We found that $Rh(NN^F)$ complexes in water lead to a flatter thermodynamic profile than in TFAH, increased transition state energies for methane activation, and decreased transition state energies for functionalization. We can understand these changes in the thermodynamics by noting that hydroxo ligands' lone pairs stabilize higher oxidation states of rhodium. Overall these changes are favorable for activity, since the functionalization energy is lowered to 31.7 kcal/mol while the methane activation energy of 35.0 kcal/mol remains acceptable. Unfortunately, an aqueous solution is predicted to offer no product protection, a result consistent with the reactivity of platinum diimine catalysts [23].

We can understand the decreased barrier for S_N2 methane functionalization (III-I, III-IV-II) in terms of several factors: the increased stability of the Rh^{IV} starting material in water, the greater thermodynamic activity of water in aqueous solution (at 55 M) as opposed to the TFA anion in

Figure 3.18. The calculated free energy (at 298 K, 1 atm CH_4) of the $(NNC)Ir(TFA)_2$ system, *via* the same internal substitution mechanism applied to Rh^{III} complexes.

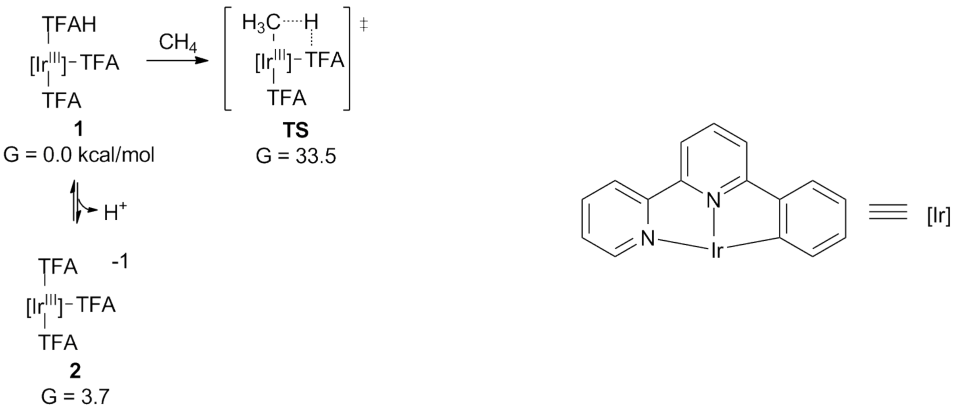

TFAH, and the fact that the transition state involves a concerted reaction featuring simultaneous formation of a C−O bond, deprotonation to form neutral methanol, and protonation of a hydroxo ligand on the Rh complex. However, we remain unclear about the reason behind the decreased S_R2 functionalization barrier for III-II. We speculate that, since some transition states for S_N2 attack by $OVCl_3$ (to form $Me{-}OVCl_3^-$) were found and appear to be about 10 kcal/mol higher than their S_R2 equivalents, there may be nucleophilic character on the oxygen atom in $OVCl_3$ S_R2 attack as well.

The most important hurdle that must be cleared experimentally in order for us to have a viable catalytic system is catalyst stability. The trend we have observed, that Rh^{III} complexes with less electron-donating ligands tend to have lower activation and functionalization barriers, must be balanced with the consideration that a ligand that is too electron-poor may not have sufficient binding strength for a stable complex with rhodium to be made. The next logical step of our investigation is the experimental synthesis and stability study of the $Rh^{III}(NN^F)$ and Rh^{III}(bisq) complexes. However, even if we fail to see good robustness for this particular complex, our more valuable contribution is that we have undertaken the most detailed *ab initio* study of the requirements of a Rh methane activation catalyst to date.

3.6 Conclusions

In our QM virtual screening of potential methane to methanol catalysts, we identified the $Rh(NN^F)$ and Rh(bisq) complexes as highly promising candidates. Features of the $Rh(NN^F)$ complex include:

- Transition state barriers for methane activation at 298 K of 27.6 (TFAH) and 35.0 kcal/mol (water), and
- Transition state barriers for functionalization at 298 K of 36.8 (TFAH) or 31.7 kcal/mol (water),

and features of the Rh(bisq) complex include:

- Transition state barriers for methane activation at 298 K of 33.4 (TFAH), and
- Transition state barriers for functionalization at 298 K of 32.0 (TFAH).

These results are better than any other $\mathrm{Rh}^{\mathrm{III}}$ complex we have so far investigated.

Moreover, we provide a rational accounting for the role that ligand design plays in the effectiveness of this promising catalyst. In particular for $\mathrm{Rh}^{\mathrm{III}}$ complexes with neutral methane activation transition states, increased electron-withdrawing ligands leads to lower barriers for both activation and functionalization. We can estimate the overall transition state barrier by simply calculating the $\mathrm{Rh}^{\mathrm{III}}-\mathrm{Me}$ species and extracting the $\mathrm{Rh}-\mathrm{C}$ bond energies. Thus, the only condition opposing even less donating ligands (i.e. lower barriers) is catalyst stability. For the $\mathrm{Rh}^{\mathrm{III}}(\mathrm{bisq}^{x})$ family of complexes, requiring one coordination site to be a weak η^2-benzene interaction greatly facilitates functionalization on a methyl group *trans* to it. These results from QM virtual screening are now ready for experimental testing, validation, and improvement. It can also be anticipated that future design of addition ligands may incorporate both concepts, with a weak interaction as well as an anionic or bidentate ligand, so that both activation barriers can be easily prediction and functionalization barriers minimized.

3.7 Acknowledgments

This work was supported as part of the Center for Catalytic Hydrocarbon Functionalization, an Energy Frontier Research Center funded by the U.S. Department of Energy, Office of Science, Office of Basic Energy Sciences under Award Number DOE DE-SC0001298.

3.8 References

[1] Cheng, W-H.; Kung, H. H. *Methanol Production and Use (Chemical Industries vol. 57)*, **1994**.

[2] (a) Labinger, J. A.; Bercaw, J. E. *Nature* **2002**, *417*, 507–514;

(b) Crabtree, R. H. *J. Chem. Soc., Dalton Trans.* **2001**, 2437–2450;

(c) Labinger, J. A. *Fuel Proc. Technol.* **1995**, *42*, 325–338;

(d) Labinger, J. A. *J. Mol. Catal. A: Chem.* **2004**, *220*, 27–35.

[3] (a) Muehlhofer, M.; Strassner, T.; Hermann, W. A. *Angew. Chem. Int. Ed.* **2002**, *41*, 1745–1747;

(b) Sen, A.; Benvenuto M. A.; Lin M. R.; Hutson A. C.; Basickes N. *J. Am. Chem. Soc.* **1994**, *116*, 998–1003.

[4] (a) Arndtsen, B. A.; Bergman, R. G.; Mobley, T. A.; Peterson, T. H. *Acc. Chem. Res.* **1995**, *28*, 154–162;

(b) Hanson, S. K.; Heinekey, D. M.; Goldberg, K. I. *Organometallics* **2008**, *27*, 1454–1463;

(c) Evans, M. E.; Jones, W. D. *Organometallics* **2011**, *30*, 3371–3377;

(d) Zakzeski, J. J.; Bell, A. T. *J. Mol. Cat. A: Chem.* **2007**, *276*, 8–16;

(e) Zhang, X. X.; Wayland, B. B. *J. Am. Chem. Soc.* **1994**, *116*, 7897–7898;

(f) Tenn, W. J. III; Conley, B. L.; Bischof, S. M.; Periana, R. A. *J. Organomet. Chem.* **2011**, *696*, 551–558;

(g) Rhinehart, J. L.; Manbeck, K. A.; Buzak, S. K.; Lippa, G. M.; Brennessel, W. W.; Goldberg, K. I.; Jones, W. D. *Organometallics* **2012**, *31*, 1943–1952;

(h) Li, L.; Brennessel, W. W.; Jones, W. D. *Organometallics* **2009**, *28*, 3492–3500;

(i) Kloek, S. M.; Heinekey, D. M.; Goldberg, K. I. *Angew. Chem. Int. Ed.* **2007**, *46*, 4736–4738.

[5] Jaguar, version 7.6; Schrödinger, LLC: New York, NY, **2007**.

[6] (a) Tannor, D. J.; Marten, B.; Murphy, R.; Friesner, R. A.; Sitkoff, D.; Nicholls, A.; Ringnalda, M.; Goddard, W. A.; Honig, B. *J. Am. Chem. Soc.* **1994**, *116*, 11875–11882;

(b) Marten, B.; Kim, K.; Cortis, C.; Friesner, R. A.; Murphy, R. B.; Ringnalda, M. N.; Sitkoff, D.; Honig, B. *J. Phys. Chem.* **1996**, *100*, 11775–11788.

[7] (a) Becke, A. D. *Phys. Rev. A* **1998**, *38*, 3098–3100;

(b) Becke, A. D. *J. Chem. Phys.* **1993**, *98*, 5648–5652;

(c) Lee, C. T.; Yang, W. T.; Parr, R. G. *Phys. Rev. B* **1988**, *37*, 785–789.

[8] (a) Zhao, Y.; Truhlar, D. G. *Theor. Chem. Acc.* **2008**, *120*, 215–241;

(b) Zhao, Y.; Truhlar, D. G. *Acc. Chem. Res.* **2008**, 41, 157–167.

[9] Hay, P. J.; Wadt, W. R. *J. Chem. Phys.* **1985**, *82*, 299–310.

[10] Martin, J. M. L.; Sundermann, A. *J. Chem. Phys.* **2001**, *114*, 3408–3420.

[11] (a) Hehre, W. J.; Ditchfield, R; Pople, J. A. *J. Chem. Phys.* **1972**, *56*, 2257–2261;

(b) Francl, M. M.; Pietro, W. J.; Hehre, W. J.; Binkley, J. S.; Gordon, M. S.; Defrees, D. J.; Pople, J. A. *J. Chem. Phys.* **1982**, *77*, 3654–3665.

[12] (a) Clark, T.; Chandrasekhar, J.; Spitznagel, G. W.; Schleyer, P. V. *J. Comput. Chem.* **1983**, *4*, 294–301;

(b) Krishnan, R.; Binkley, J. S.; Seeger, R.; Pople, J. A. *J. Chem. Phys.* **1980**, *72*, 650–654.

[13] Pipek, J.; Mezey, P. G. *J. Chem. Phys.* **1989**, *90*, 4916–4926.

[14] Kelly, C. P.; Cramer, C. J.; Truhlar, D. G. *J. Phys. Chem. B* **2006**, *110*, 16066–16081.

[15] Tissandier, M. D.; Cowen, K. A.; Feng, W. Y.; Gundlach, E.; Cohen, M. H.; Earhart, A. D.; Coe, J. V.; Tuttle, T. R. *J. Phys. Chem. A* **1998**, *102*, 7787–7794. Calculated at standard conditions.

[16] Wertz, D. H. *J. Am. Chem. Soc.* **1980**, *102*, 5316–5322.

[17] Wagman, D. D.; Evans, W. H.; Parker, V. B.; Schumm, R. H.; Halow, I.; Bailey, S. M.; Churney, K. L.; Nuttall, R. L. *J. Phys. Chem. Ref. Data* **1982**, *11*, 1–14.

[18] For trifluoroacetic acid: Kreglewski, A. *Bull. Acad. Pol. Sci. Ser. Sci. Chim.* **1962**, *10*, 11-12, 629–633.

For water: (a) Bridgeman, O.C.; Aldrich, E.W. *J. Heat Transfer* **1964**, *86*, 279–286;

(b) Liu, C.-T.; Lindsay, W.T., Jr. *J. Chem. Eng. Data* **1970**, *15*, 510–513.

[19] Holleman, A. F.; Wiberg, E.; Wiberg, N. *Lehrbuch der Anorganischen Chemie*, (91–100 ed.;) Walter de Gruyter, **1985**; pp. 1056–1057.

[20] Goldberg, K. I.; Yan, J. Y.; Breitung, E. M. *J. Am. Chem. Soc.* **1995**, *117*, 6889–6896.

[21] Cheng, M. J., Nielsen, R. J., Goddard, W.A. Manuscript under preparation.

[22] Using $k = \frac{k_B T}{h} \cdot \exp\left(\frac{-\Delta G^\ddagger}{k_B T}\right)$.

[23] Owen, J. S.; Labinger, J. A.; Bercaw, J. E. *J. Am. Chem. Soc.* **2006**, *128*, 2005–2016.

[24] Periana, R. A.; Taube, D. J.; Evitt, E. R.; Loffler, D. G.; Wentrcek, P. R.; Voss, G.; Masuda, T. *Science* **1993**, *259*, 340–343.

[25] Periana, R. A.; Taube, D. J.; Gamble, S.; Taube, H.; Satoh, T.; Fujii, H. *Science* **1998**, *280*, 560–564.

[26] Anslyn, E.; Dougherty, D. *Modern Physical Organic Chemistry*; University Science Books, **2006**.

[27] Young, K. J. H.; Oxgaard, J.; Ess, D. H.; Meier, S. K.; Stewart, T.; Goddard, W. A.; Periana, R. A. *Chem. Commun.* **2009**, 3270–3272.

[28] According to transition state theory, the activation energy $\Delta G^\ddagger$ may be derived from the turnover frequency TOF using the formula $\mathrm{TOF} = \frac{k_B T}{h} \cdot \exp\left(\frac{-\Delta G^\ddagger}{k_B T}\right)$.